J. Fluid Mech. (2007), *vol.* 583, *pp.* 379–412.
doi:10.1017/S0022112007006325 Printed in the United Kingdom

Inertial instability in rotating and stratified fluids: barotropic vortices

R. C. KLOOSTERZIEL[1] G. F. CARNEVALE[2] AND P. ORLANDI[3]

[1]School of Ocean & Earth Science & Technology, University of Hawaii, Honolulu, HI 96822, USA
[2]Scripps Institution of Oceanography, University of California, San Diego, La Jolla, CA 92093, USA
[3]Dipartimento di Meccanica e Aeronautica, University of Rome, "La Sapienza," via Eudossiana 18, 00184 Roma, Italy

(Received 30 May 2006 and in revised form 2 March 2007)

The unfolding of inertial instability in intially barotropic vortices in a uniformly rotating and stratified fluid is studied through numerical simulations. The vortex dynamics during the instability is examined in detail. We demonstrate that the instability is stabilized via redistribution of angular momentum in a way that produces a new equilibrated barotropic vortex with a stable velocity profile. Based on extrapolations from the results of a series of simulations in which the Reynolds number and strength of stratification are varied, we arrive at a construction based on angular momentum mixing that predicts the infinite-Reynolds-number form of the equilibrated vortex toward which inertial instability drives an unstable vortex. The essential constraint is conservation of total absolute angular momentum. The construction can be used to predict the total energy loss during the equilibration process. It also shows that the equilibration process can result in anticyclones that are more susceptible to horizontal shear instabilities than they were initially, a phenomenon previously observed in laboratory and numerical studies.

1. Introduction

Centrifugal instability was first investigated by Rayleigh (1916). He showed that a steady, circularly symmetric, inviscid swirling flow with swirling velocity $V(r)$ is unstable when the magnitude of angular momentum $L = Vr$ decreases with increasing radius r in some region of the flow. The criterion for instability is that the Rayleigh discriminant $\Phi < 0$ where

$$\Phi = \frac{1}{r^3}\frac{\mathrm{d}L^2}{\mathrm{d}r} = \frac{1}{r^3}\frac{\mathrm{d}(Vr)^2}{\mathrm{d}r} \tag{1.1}$$

(see figure 1*a* for symbol definitions). He used an energy argument, imagining two fluid rings of equal volume to exchange positions in a homogeneous fluid while preserving angular momentum. If both rings are within the domain where $\Phi < 0$, the change in kinetic energy of the two fluid rings is negative and hence energy is liberated which implies instability. For a given velocity $V(r)$ there is a balance between the centrifugal force V^2/r and the radial pressure gradient $\partial_r p$. A single fluid ring, being displaced a small distance δr from its original position, conserving its angular momentum (or circulation) while leaving the pressure field unchanged, will accelerate whenever $\Phi < 0$ at its original location. However, if $\Phi > 0$ it will tend to return to its original location. In this sense the instability can be viewed as due

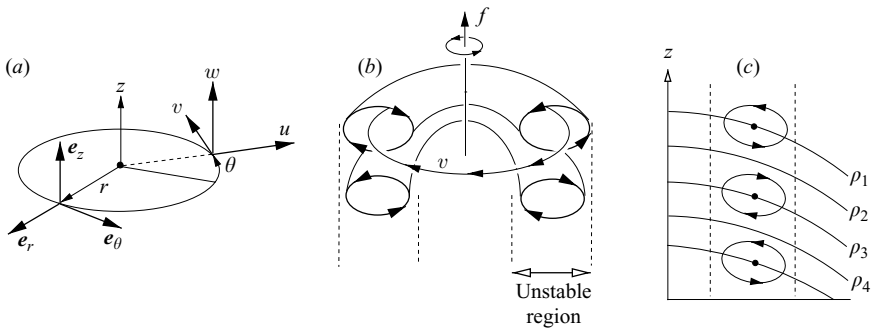

FIGURE 1. (*a*) Diagram defining the polar coordinate system and velocity components for a circular vortex; v is the swirl velocity, w the vertical velocity component and u the radial velocity component. (*b*) Inertial instability starts in an unstable region as toroidal vortices ('rib vortices') of alternating sign. (*c*) Side view indicating that in a stratified environment lateral and vertical mixing of density may occur.

to an unstable balance between the centrifugal force and the pressure gradient. The instability manifests itself as overturning motions in the meridional (r, z)-plane (see figure 1*b*). In Taylor–Couette flow these motions are the well-known toroidal vortices observed in a fluid contained in between two rotating concentric cylinders when $\Phi < 0$ (Drazin & Reid 1981).

In an attempt to explain the great difficulty in creating stable anticyclones in a rotating homogeneous fluid, Kloosterziel & van Heijst (1991) extended Rayleigh's criterion and found that the Rayleigh discriminant becomes

$$\Phi = \frac{1}{r^3}\frac{\mathrm{d}L^2}{\mathrm{d}r} = \frac{2L}{r^2}\frac{1}{r}\frac{\mathrm{d}L}{\mathrm{d}r} = (2V/r + f)(\omega_z + f), \tag{1.2}$$

where

$$L = Vr + \frac{1}{2}fr^2 \quad \text{and} \quad \omega_z = \frac{1}{r}\frac{\mathrm{d}Vr}{\mathrm{d}r} \tag{1.3}$$

are the absolute angular momentum (with V the (relative) velocity in the rotating reference frame) and the relative vorticity component in the z-direction (along the axis of rotation), respectively; f is the Coriolis parameter. Equation (1.2) can be found in Sawyer (1947). In the older meteorological literature it is also called 'dynamic instability', 'inertial instability' when formulated in terms of motions in a rotating frame of reference and 'symmetric instability' because the perturbations are axisymmetric or invariant in the basic flow direction.

While (1.1) and (1.2) apply to homogeneous and incompressible fluids, Solberg (1936) considered the far more complicated question of the stability of atmospheric compressible zonal flows circulating about the Earth with no variation with longitude. Solberg used a 'displaced ring' argument which leads to the criterion for instability

$$\frac{2L}{r^2}Q = \left(\frac{2V}{r} + f\right)Q < 0, \tag{1.4}$$

where Q is the Ertel potential vorticity. In an inviscid adiabatic fluid the potential vorticity is conserved, i.e. $\mathrm{D}Q/\mathrm{D}t = 0$, as is absolute angular momentum when the flow remains circularly symmetric, i.e. $\mathrm{D}L/\mathrm{D}t = 0$. Under such circumstances the product LQ is conserved, as well as its sign which determines stability. Hence, in order to

reach a stable equilibrium, viscous and diffusive effects are required to break the constraints of angular momentum and potential vorticity conservation.

Here we extend our earlier work (Carnevale *et al.* 1997; Orlandi & Carnevale 1999) on the (in)stability of barotropic circular vortices in rotating homogeneous fluids to such vortices embedded in uniformly stratified fluids. In this case the criterion (1.4) corresponds to $\Phi < 0$ if we identify Q with absolute vorticity, that is $Q = \omega_z + f$. With fully nonlinear simulations, we investigate the unfolding of the instability in both anticyclones and cyclones. They are subjected to Coriolis forces represented by a constant Coriolis parameter f and the environment has constant buoyancy frequency N. Unlike in our earlier studies (which were fully three-dimensional), here we only allow purely symmetric evolutions, thus isolating the effects of pure inertial instability from other possible instabilities that may occur. We look at questions such as: In the linear stage what is the preferred (fastest growing) vertical scale as a function of the Reynolds number Re and the stratification (as measured by N)? Does the nonlinear evolution reach a steady state and if so what is this state and how does it differ from the initial state? What can one say about the stability of the final state? How much energy is lost during the unfolding of the instability due to dissipation, density mixing and internal wave radiation? This study is an attempt to answer such questions. Some of our findings are analogous to those found in previous studies of different types of flows and when appropriate this will be noted.

In § 2 we first discuss some pertinent linear theory. In § 3 we outline the numerical model, the boundary conditions and the model vortices. In § 4 we proceed with a detailed example of the unfolding of the instability in a particular anticyclone. This is just one example of many simulations that form the basis for the results presented in § 5 and § 6. In § 4 we discuss, in addition to the evolution of the basic flow, the accompanying density mixing and internal wave radiation. In § 5 we continue with a systematic study of the instability of an anticyclone with particular emphasis on the variations with Re and N. For a limited range (limited by computational feasibility) of either parameter, we determine the preferred vertical scales of the instability and growth rates in the early stages of the evolution. After the linear stage of the unfolding of the instability, the highly nonlinear stage is studied in which the initially regular 'stacks' of overturning cells become highly distorted and start to move out of the region of instability (where $\Phi < 0$) into the inertially stable regions. These outward and inward motions advect and mix absolute angular momentum L. Ultimately a new vortex appears and we present evidence that for increasing Re the final (inertially stable) vortex tends to be in solid-body rotation in its core but motion rapidly decreases beyond its position of peak velocity. This solid-body rotation corresponds to $L \approx 0$ which is the result of mixing equal amounts of both positive and negative L while preserving total L. We then offer our first hypothesis regarding the expected final velocity profiles for very high Reynolds numbers and the energy losses one may expect due to inertial instability.

In § 6 we study the unfolding of the instability in cyclones. After first discussing again the scale selection and growth rates in the linear stage of the evolution, we study the equilibrated cyclones that result from the instability. Here we find that the absolute angular momentum is mixed to an approximately constant positive value L_c by the instability. The range over which this happens generally does not penetrate all the way to the centre of the vortex. We offer our second hypothesis regarding the expected final velocity profiles for very high-Reynolds-number cyclones and the energy losses one may expect due to inertial instability. In § 7 we summarize the main results.

2. Linear theory

For an incompressible fluid, in cylindrical coordinates the governing equations on the f-plane with the Boussinesq approximation are

$$\frac{\partial u}{\partial t} + \boldsymbol{u}\cdot\nabla u - \frac{v^2}{r} - fv = -\frac{1}{\rho_0}\frac{\partial p}{\partial r} + \nu\left(\nabla^2 u - \frac{u}{r^2} - \frac{2}{r^2}\frac{\partial v}{\partial \theta}\right), \tag{2.1}$$

$$\frac{\partial v}{\partial t} + \boldsymbol{u}\cdot\nabla v + \frac{uv}{r} + fu = -\frac{1}{\rho_0 r}\frac{\partial p}{\partial \theta} + \nu\left(\nabla^2 v - \frac{v}{r^2} + \frac{2}{r^2}\frac{\partial u}{\partial \theta}\right), \tag{2.2}$$

$$\frac{\partial w}{\partial t} + \boldsymbol{u}\cdot\nabla w - b = -\frac{1}{\rho_0}\frac{\partial p}{\partial z} + \nu\nabla^2 w, \tag{2.3}$$

$$\frac{\partial b}{\partial t} + \boldsymbol{u}\cdot\nabla b + N^2 w = \kappa\nabla^2 b, \tag{2.4}$$

$$\frac{1}{r}\frac{\partial (ru)}{\partial r} + \frac{1}{r}\frac{\partial v}{\partial \theta} + \frac{\partial w}{\partial z} = 0. \tag{2.5}$$

Here the Laplace operator, the gradient and $\boldsymbol{u}$ are

$$\nabla^2 = \frac{1}{r}\frac{\partial}{\partial r}r\frac{\partial}{\partial r} + \frac{1}{r^2}\frac{\partial^2}{\partial \theta^2} + \frac{\partial^2}{\partial z^2}, \quad \nabla = \boldsymbol{e}_r\frac{\partial}{\partial r} + \boldsymbol{e}_\theta\frac{1}{r}\frac{\partial}{\partial \theta} + \boldsymbol{e}_z\frac{\partial}{\partial z}, \quad \boldsymbol{u} = \boldsymbol{e}_r u + \boldsymbol{e}_\theta v + \boldsymbol{e}_z w \tag{2.6}$$

(see figure 1a for symbol definitions). In the above equations the total density ρ has been decomposed into a background stratification $\bar{\rho}(z)$ and a perturbation ρ', while with the Boussinesq approximation the total density $\bar{\rho} + \rho'$ has been replaced in (2.1)–(2.3) by a constant reference density ρ_0 where it appears in the denominators. $b = -g\rho'/\rho_0$ is the buoyancy and $N^2 = -(g/\rho_0)\mathrm{d}_z\bar{\rho}(z)$ the square of the buoyancy frequency with g the gravitational constant. The kinematic viscosity ν and diffusivity κ will be assumed constant. The pressure p is the deviation from the background hydrostatic pressure.

Setting $\nu = \kappa = 0$, consider a steady barotropic vortex $v = V(r)$ that is in cyclo-geostrophic balance

$$\frac{V^2}{r} + fV = \frac{1}{\rho_0}\frac{\mathrm{d}P}{\mathrm{d}r}, \tag{2.7}$$

while u, w, $\rho' = 0$. In (2.7) the pressure $p = P(r)$. Introducing perturbations u', v', w', ρ' and p' independent of the azimuthal angle θ and linearizing (2.1)–(2.5) about the balanced state (2.7) a set of equations follows with which one can show that (Kloosterziel & Carnevale, unpublished manuscript)

$$\frac{\mathrm{d}}{\mathrm{d}t}\frac{1}{2}\iiint \rho_0\left(u'^2 + \frac{(2V/r + f)^2}{\Phi}v'^2 + w'^2 + \frac{b^2}{N^2}\right)\mathrm{d}\mathscr{V} = 0, \tag{2.8}$$

where $\mathrm{d}\mathscr{V} = r\,\mathrm{d}r\,\mathrm{d}z\,\mathrm{d}\theta$ stands for the volume integral over the domain and Φ is the Rayleigh discriminant (1.2). Equation (2.8) is valid for flows bounded above and below by horizontal rigid boundaries so that w' vanishes there. We can consider either a cylindrical vertical rigid wall far from the vortex where u' would have to vanish or a horizontally unbounded domain and require that u' vanishes 'fast enough' for $r \to \infty$.

Considering only statically stable background stratification ($N^2 > 0$), we see that if $\Phi > 0$ everywhere, the flow is linearly stable. If $\Phi < 0$ in some region, there may be instability since u', v', w' and b can grow without bounds without violating the conservation law (2.8). There are at least three other ways to prove linear stability when $N^2 > 0$ and $\Phi > 0$: by extending Rayleigh's (1916) ring exchange argument

to stratified rotating fluids, by using Solberg's (1936) 'displaced ring' argument or by Ooyama's (1966) method which is based on Fjørtoft's (1950) 'energy method'. We believe (2.8) is a novel and elegant addition to these alternatives. It should be remembered that stability is only established with respect to circularly symmetric perturbations. Vortices with $\Phi > 0$ everywhere (inertially stable) may be unstable to barotropic instabilities, i.e. horizontal shear instabilities that involve θ-variations (see for example Carton & McWilliams 1989; van Heijst, Kloosterziel & Williams 1991; Carnevale & Kloosterziel 1994). Recently, Billant & Gallaire (2005) established analytically with a normal modes analysis that for a class of inertially unstable vortices, generally in the linearized dynamics the circularly symmetric (inertial) instabilities are the most dangerous, that is, their growth rates exceed those of non-axisymmetric instabilities (see also Gallaire & Chomaz 2003).

If one writes $u' = \partial_z \psi$, $w' = -1/r \partial_r r\psi$, a single equation (the so-called Eliassen–Sawyer equation) can be derived for the meridional streamfunction ψ (see for example Hua, Moore & Le Gentil 1997*b* where this is done for a parallel shear flow on the equatorial β-plane). Assuming normal-mode solutions of the form $\psi = \exp(st)\Psi(r, z)$ exist, with $\psi = 0$ at the top and the bottom and also at $r = 0$ and in the limit $r \to \infty$, one finds that

$$\iiint \left[(s^2 + N^2) \left| \frac{1}{r} \frac{\partial \Psi r}{\partial r} \right|^2 + (s^2 + \Phi) \left| \frac{\partial \Psi}{\partial z} \right|^2 \right] \mathrm{d}\mathscr{V} = 0. \tag{2.9}$$

This is valid for any $N^2(z)$ and $\Phi(r)$ (Kloosterziel & Carnevale, unpublished manuscript). Thus it is seen that if $\Phi < 0$ in some region, then $s < |\Phi|_{\mathrm{m}}^{1/2}$, where $|\Phi|_{\mathrm{m}} = \max\{-\Phi\}$. That is, $|\Phi|_{\mathrm{m}}^{1/2}$ is the upper limit for the growth rates, for any $N^2 \geqslant 0$. If $N^2 = \text{constant}$, normal modes solutions are allowed with $\psi = \exp(st) \sin(m\pi z/H)\Psi_m(r)$ with the bottom at $z = 0$ and the top at $z = H$ and $m = 1, 2, \ldots$. One then finds that at the transition from stability to instability ($s = 0$), Ψ_m satisfies a simple equation which shows that there is a critical vertical wavenumber $m = m_c$ (the vertical cutoff wavenumber) so that for $m > m_c$ there will be instability, for $m < m_c$ stability. Further one finds that $m_c \propto N$. An early study where this was first explicitly shown is that of Yanai & Tokiaka (1969). That for given N^2 there is a threshold vertical scale above which no growth occurs and that this scale decreases with increasing N^2 (the vertical cutoff scale introduced above) can be understood as follows: the meridional motions extract energy from the basic azimuthal flow $V(r)$, which leads to their growth. However, any vertical motion in the stratified fluid requires work or, in other words, this absorbs some of the liberated energy. Therefore higher growth rates are associated with 'flatter' secondary motions in the meridional plane. Generally for $m \to \infty$ the highest growth rate, $s = |\Phi|_{\mathrm{m}}^{1/2}$, is attained. This was probably first shown by Stone (1966) for a vertically sheared flow and Yanai & Tokiaka (1969) for a horizontally sheared flow on the f-plane. Normal modes analysis (numerical) by Smyth & Peltier (1994 and references therein) and Smyth & McWilliams (1998) for barotropic vortices also showed that maximum growth rates are attained at vanishing vertical scales. Billant & Gallaire (2005) established this analytically with a normal modes analysis for a number of different types of vortices in a rotating stratified fluid.

As mentioned above, for given stratification, only below a certain cutoff vertical scale will growth occur in the inviscid limit. But, since viscosity preferentially damps smaller scales, for increasing stratification this cutoff scale may become so small that no growth will occur. Thus, for finite Reynolds numbers Re, $\Phi < 0$ is

necessary for instability but not sufficient. Only for sufficiently high $Re > Re_c$ can the instability proceed, and this critical Reynolds number Re_c will increase with increasing stratification. Further, since for given N^2 and any given Re no growth will occur when m is below the cutoff wavenumber while for $m \to \infty$ viscous effects will completely damp growth of high-m-modes, there will be a finite range of vertical wavenumbers that can exhibit growth if N^2 is not too large. (In an analysis of an isolated vortex in a homogeneous, non-rotating fluid, Gallaire & Chomaz (2003) claim that the upper limit of this range is $m \propto \sqrt{|\Phi|_{\mathrm{m}} Re}$). Within this range a maximum growth rate will be found at a specific vertical wavenumber. Hence, a scale selection will occur in the sense that if the system is subjected to a small perturbation and this 'fastest' mode is excited, one expects this scale after some time to dominate in the meridional flow field if the growth rates for neighbouring wavenumbers are well-separated. Generally one can expect the maximum growth rate and the associated wavenumbers m to increase with Re. Griffiths (2003*a*) showed this for general parallel shear flows on the equatorial β-plane (albeit with the hydrostatic approximation and ignoring horizontal diffusion). Gallaire & Chomaz (2003) established it numerically for a variety of isolated vortices in a non-rotating homogeneous fluid. For fixed Re, a change in N^2 must also affect the maximum growth rate and the corresponding vertical scale, but in what way is hard to predict. Generally (see for example Potylitsin & Peltier 1998; Griffiths 2000*b*) for fixed Re, an increase in N^2 decreases the maximum growth rate while the associated vertical wavenumber increases, neither of which is surprising since the higher N, the more energetically costly will be vertical excursions. Thus increasing N decreases the vertical wavelength of the instability.

3. Numerical model and simplifying assumptions

The unfolding of inertial instability in a vortex is investigated with the use of a numerical model. The evolution of the vortex was simulated with a Navier–Stokes code in the Boussinesq approximation, i.e. equations (2.1)–(2.5). We only consider $\bar{\rho}(z)$ linear in z so that N^2 is constant. The domain is of finite height, enclosed by a horizontal lower rigid boundary at $z = 0$ and an upper rigid lid at some finite height $z = H$. For the vertical velocity the boundary condition there is $w = 0$ (no-flux condition). Free-slip boundary conditions are used at the top and bottom boundaries, that is, we set $\partial_z u = \partial_z v = 0$ there. In Orlandi & Carnevale (1999) we investigated how the presence of an Ekman bottom boundary layer changes the stability of barotropic vortices. Here we isolate the effect of inertial instability from that effect by using the free-slip condition. In the horizontal r-direction the domain is terminated by a rigid vertical cylindrical wall at some finite radius $r = R$. There $u = 0$ (no flux) and free slip is used again, i.e. $\partial_r w = 0$ and $\partial v/\partial r - v/r = 0$. With free-slip boundary conditions equation (2.2) implies that the total absolute momentum ($L_{\mathrm{tot}} = \iiint L \, \mathrm{d}\mathscr{V}$) is conserved ($\mathrm{d}L_{\mathrm{tot}}/\mathrm{d}t = 0$), where L is defined in (1.3). The boundary condition for the density field at the top and bottom is the no-flux condition $\partial_z \rho' = 0$. Similarly, we take $\partial_r \rho' = 0$ at $r = R$.

The code uses a second-order-accurate finite-difference staggered-mesh scheme in a cylindrical coordinate system. The details of the method are explained in Orlandi (2000). The code allows arbitrary stretching in the radial and vertical directions. We concentrated our grid points in and around the instability region. This region can be expected to be where $\Phi < 0$. The number of gridpoints in the azimuthal (θ) direction was set to one, so that no azimuthal variations in the various fields are allowed to develop. Thus these are simulations of axisymmetric flows.

All results shown below had a resolution of 257×257 in the meridional (r, z) plane. All of the results presented were also checked against those from simulations with 129×129 gridpoints (some with 353×353 gridpoints). We found that the 257×257 resolution was adequate for the present purpose of examining a large range of parameter space with many simulations. For example, we checked how results varied with vertical resolution for a case with the highest stratification used ($N^2 = 50$), which theoretically gives the strongest vertical variations. Comparing growth rates at $N^2 = 50$ showed that the 257×257 case gave an accuracy of 0.3 % compared to the higher resolution case, and 3 % compared to the lower resolution test. In terms of determining the wavenumber of the fastest growing modes, the tests showed 257×257 resolution gave the wavenumber accurate to better than 3 %. This and other tests involving the fall-off of the energy spectrum with wavenumber provide confidence in the data presented within the ranges of Re and N discussed.

In the discussion that follows all dimensional quantities are reported in non-dimensional form where the time scale is f^{-1} and the length scale is L_h, the horizontal scale of the vortex (see below). In most cases the simulations were performed on a computational domain of length $4L_\mathrm{h}$ in the radial direction and $H = L_\mathrm{h}$ in the vertical. The bottom is at $z = 0$ and non-dimensionally the top is at $z = 1$. With these dimensions for the computational domain there was sufficient vertical space to allow the centrifugal instability within the vortex to fully develop. However, when investigating the radiation of internal waves by the instability, the radial extent of the domain was enlarged and a frictional Rayleigh sponge layer was added to prevent reflection of internal waves from the sidewall.

Non-dimensional parameters of importance are the Reynolds number, defined as $Re = UL_\mathrm{h}/\nu$, the Rossby number Ro (defined below), the ratio N/f and the Prandtl number $Pr = \nu/\kappa$. We have mainly restricted considerations to one particular profile and only a few Rossby numbers that guaranteed inertial instability. In all the simulations we set the Prandtl number equal to one. Values of N/f or N^2/f^2 will be denoted by N or N^2, respectively.

The velocity profile for the barotropic circular vortices that we will study is taken from a family of profiles parameterized by the steepness of the fall-off of the velocity field. They are

$$V(r) = U v_\alpha(r), \quad v_\alpha(r) = r^{\alpha/2} \exp\left(-\tfrac{1}{2} r^\alpha + \tfrac{1}{2}\right) \tag{3.1}$$

where $\alpha > 0$ is the steepness parameter. The radius r has been non-dimensionalized with the horizontal length scale L_h. For all α, $v_\alpha(r = 1) = 1$, which is its peak value (see figure 2*a*). Note that the velocity profile, after reaching its peak, falls off faster to zero for larger α, which is what we mean by 'steeper'. U is a velocity amplitude. The relative vorticity ω_z for this profile at $r = 0$ is non-zero if we choose $\alpha = 2$ but vanishes for $\alpha > 2$. Thus with this family we can cover both these situations. Most detailed results presented below are from simulations with vortices with $\alpha = 3$ since no essential difference in the evolution is observed between the $\alpha = 2$ and $\alpha = 3$ vortices But some results for $\alpha = 2$ and other types of vortices are mentioned in § 5.3 and shown in § 7.

In the simulations we took f positive, so $U > 0$ corresponds to a cyclone, $U < 0$ to an anticyclone. The Rossby number is based on the peak velocity U, which occurs at a distance L_h from the centre, i.e. we define $Ro = U/fL_\mathrm{h}$, which is positive for cyclones, and negative for anticyclones.

Non-dimensionally the Rayleigh discriminant (1.2) is

$$\Phi = (2Ro\, v_\alpha/r + 1)(Ro\, \omega_z + 1), \quad \omega_z = (1/r)\mathrm{d}_r(r v_\alpha). \tag{3.2}$$

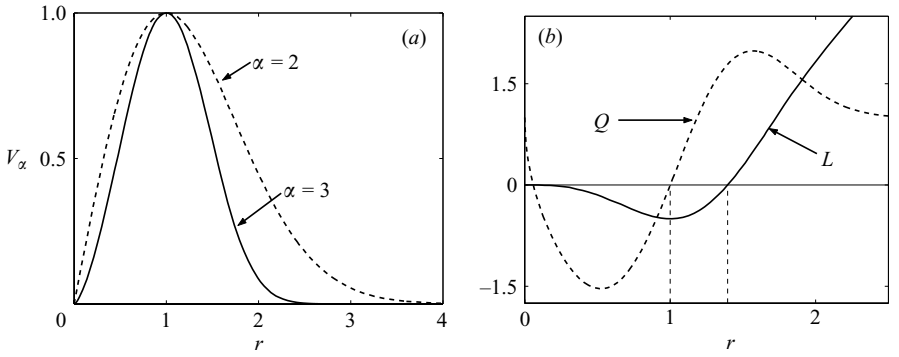

FIGURE 2. (*a*) The velocity profile $v_\alpha(r)$ for $\alpha = 2$ and 3. (*b*) The absolute angular momentum L (solid line) and absolute vorticity Q (dashed line) for the case $\alpha = 3$ and $Ro = -1$. The Rayleigh discriminant $\Phi = (2L/r^2)Q \leqslant 0$ for a range of r-values indicated by vertical dashed lines (between $r = 1$ and $r \approx 1.4$). In this range $L \leqslant 0$ and $Q \geqslant 0$. The minimum value of Φ is -0.56 thus $|\Phi|_{\mathrm{m}}^{1/2} = 0.75$ (the upper limit for the inviscid growth rate). When $Ro > -0.39$, $\Phi \geqslant 0$ for all r in which case both $L \geqslant 0$ and $Q \geqslant 0$.

The condition for instability in an ideal fluid ($\Phi < 0$) will be satisfied for large enough negative and positive Rossby numbers.

The instability is initiated by giving the vortex a small random perturbation, by multiplying the velocity profile (3.1) at each gridpoint by a random number of unit mean. Specifically we take the initial velocity field to be

$$v(r, z) = (1 + \eta(r, z))V(r), \tag{3.3}$$

where η is a random process of zero mean and standard deviation 10^{-3}.

4. An example of inertial instability

In this section we examine in detail a representative example of the unfolding of inertial instability of an anticyclone with the $\alpha = 3$ profile and an initial Rossby number $Ro = -1$. Instability is expected in an annulus between the dashed lines in figure 2(*b*) where Φ is negative. This region extends from the top to the bottom of the domain. The instability region is where $L < 0$ and $Q > 0$, i.e. where the Rayleigh discriminant (1.2) $\Phi = 2LQ/r^2 < 0$. Although strictly speaking $Q = N^2(\omega_z + f)$ when there is no vertical shear, we will refer to $\omega_z + f$ as the potential vorticity $Q = (1/r)\mathrm{d}L/\mathrm{d}r$ since $N^2 = \text{constant}$.

4.1. *Angular momentum redistribution*

In figure 3, we visualize the evolution of the instability with contour plots of the azimuthal vorticity $\omega_\theta = \partial_z u - \partial_r w = 0$, which is a good diagnostic of the overturning motions in the meridional plane. In this example $N^2 = 2$ and the Reynolds number is $Re = 10^4$. The instability starts within the instability region as predicted by inviscid linear theory as discussed above (between the solid vertical lines in figure 3*a*). The signature of the linear phase of the instability is a vertical stack of elliptical regions of high values of ω_θ of alternating sign. Each of these elliptical structures corresponds to a horizontal ring of ω_θ that encircles the primary vortex. These rings are referred to as 'rib vortices'. Early in the evolution, the rings are regular and neatly aligned vertically. By $t = 15$ (figure 3*b*), nonlinear interactions lead to pairing of opposite-signed rings and this causes propagation beyond the bounds of the unstable region (figure 3*c*).

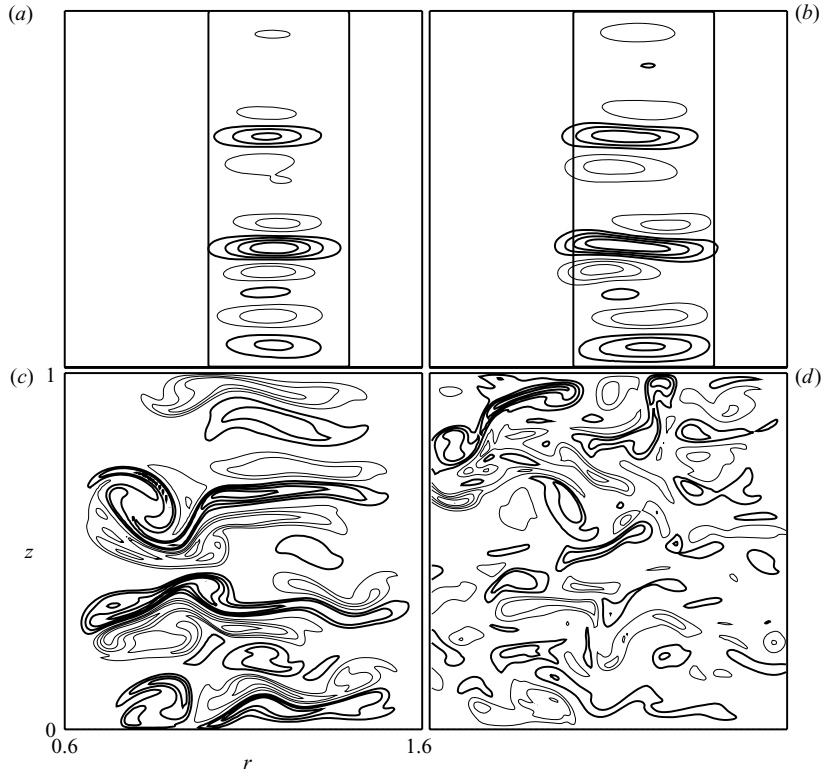

FIGURE 3. Evolution of ω_θ in a vertical cross-section for the anticyclone with $\alpha = 3$, $Ro = -1$, $N^2 = 2$ and $Re = 10^4$. Thick/thin lines are used for $+/-$ contours. The alternating sign of ω_θ indicates the alternating sense of rotation of the rib vortices that initially start in unstable regions (between the two vertical lines in (*a*) and (*b*)). The times are (*a*) $t = 10$, (*b*) $t = 15$, (*c*) $t = 20$ and (*d*) $t = 25$. The contour intervals $\Delta\omega_\theta$ for each panel are: (*a*) 0.11, (*b*) 0.75, (*c*) 1.9 (*d*) 1.8. Pairing of rib vortices leads to propagating 'dipoles' which mix angular momentum both inside and outside the initial instability domain. In each panel in the horizontal only a portion of the computational domain, which extended from $r = 0$ to $r = 4$, is shown, i.e. $0.6 \leqslant r \leqslant 1.6$.

A given vortex ring becomes part of both inwardly and outwardly propagating mushroom-shaped dipolar vortex structures. Near the inner edge of the instability region, a vortex ring with, say, positive-ω_θ pairs with the vortex below it to form an inwardly propagating dipolar vortex structure. At the same time, the part of this vortex ring that is near the outer boundary of the instability region pairs with the vortex above it to form an outwardly propagating dipolar structure. These structures propagate both inwardly and outwardly from the initial instability region into the initially stable regions. Such pairing and propagation of the meridional disturbances has previously been observed in laboratory experiments by Afanasyev & Peltier (1998) and by Griffiths (2003*b*) in a numerical study of zonal flow on the equatorial β-plane. Strong nonlinear interactions between the vortices results in the small-scale vorticity seen in figure 3(*d*). Note that in these panels the dimension of the section of the computational domain shown is the same in the vertical and horizontal directions. Thus one can appreciate the true aspect ratio of the structures and note that they are much longer in the radial than the vertical direction.

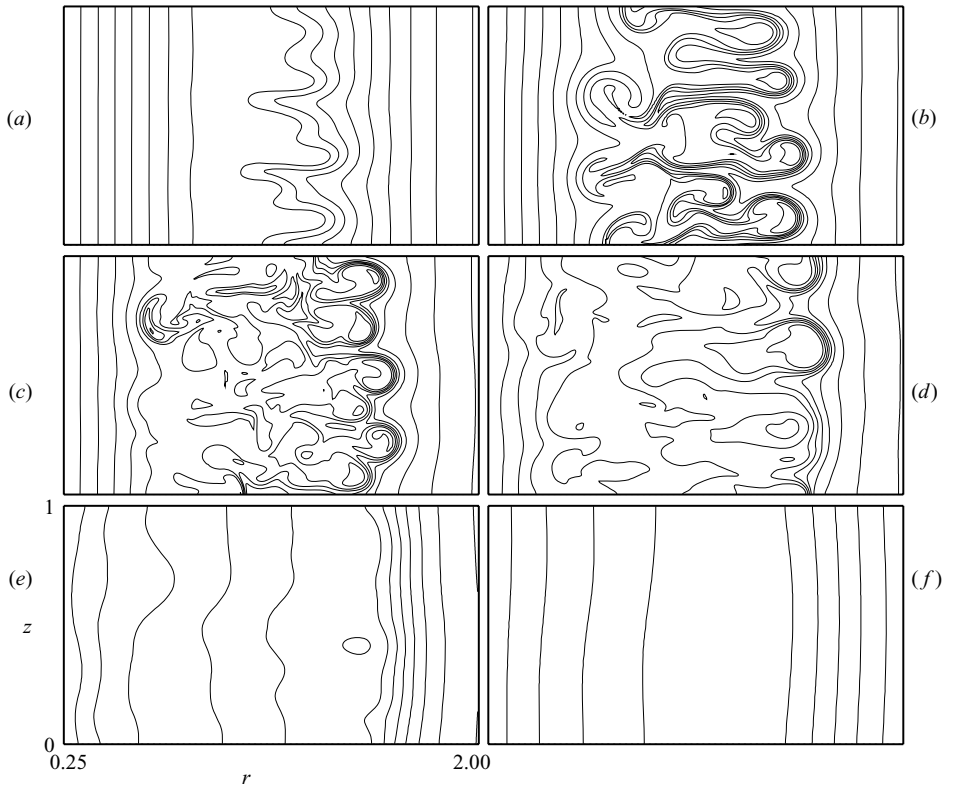

FIGURE 4. Evolution of the swirl velocity v in a vertical cross-section. ($Re = 10^4$, $N^2 = 2$). The contour interval is $\Delta v = 0.1$. The times are (*a*) $t = 15$, (*b*) $t = 20$, (*c*) $t = 25$, (*d*) $t = 35$, (*e*) $t = 80$ and (*f*) $t = 300$.

The contour plots of ω_θ give us insight into the dynamics of the instability but do not provide an idea of the degree to which the primary vortex is changed or distorted by the unfolding of the instability. The change to the primary vortex is visualized in figure 4 by showing the evolution of the contours of v. For the unperturbed barotropic vortex, the contours are vertical lines. By $t = 15$ (figure 4*a*), there is already a significant level of disturbance. At $t = 20$ (figure 4*b*), nonlinear pairing of the vortex rings has produced the characteristic mushroom shapes associated with the dipolar heads seen in figure 3(*b*). In figures 3(*c*) and 3(*d*) (times $t = 20$ and 25), it was surprising to see how much more intense the gradients of v_θ had become in the outer region (that is where r is larger than the limit of the linear instability region) than in the inner region. We checked each of the contributions to the evolution of v_θ as given by equation (2.2) against the numerical simulations and found that the advective terms at these times are far stronger than the Coriolis terms and alone are responsible for the asymmetry. By $t = 35$ (figure 4*c*) the inwardly advancing disturbance has nearly halted and the perturbation to v has weakened, while the perturbations at the outwardly propagating edge of the disturbance remain strong. By $t = 80$ (figure 4*e*), active dipolar pairs are no longer evident and the contours are relaxing toward a barotropic state. By $t = 300$ (figure 4*f*) the evolution has almost come to a halt, aside from slow oscillations within the re-formed vortex. A new stationary vortex which appears to be inertially stable has been formed.

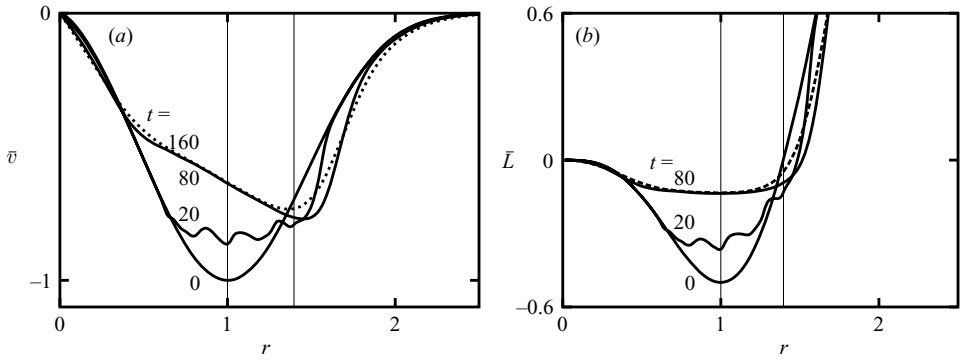

FIGURE 5. (*a*) Vertically averaged swirl velocity $\bar{v}(r,t) = \int_0^1 v(r,z,t)\mathrm{d}z$ at $t = 0$, 20 and 80 (solid curves) and $t = 160$ (dotted curve) with $Re = 10^4$ and $N^2 = 2$. At $t = 80$, when the vortex has almost reached a new quasi-steady state, the amplitude has decreased a significant amount while angular momentum mixing has significantly changed the velocity profile between a position near the centre of the vortex and beyond the outer edge of the initially unstable region. (*b*) Angular momentum $\bar{L} = \bar{v}r + \frac{1}{2}fr^2$ at the same times as (*a*). The vertical solid lines indicate the initial instability region.

A useful diagnostic of the evolution of the primary vortex is $\bar{v}(r,t) = \int_0^1 v(r,z,t)\,\mathrm{d}z$, the vertically averaged value of v. The evolution of $\bar{v}$ shown in figure 5 demonstrates that most of the deformation and re-formation of the vortex is complete by $t = 80$. The thin vertical lines in this plot indicate the initial instability region. The evolution of the profile in figure 5(*a*) from $t = 0$ to $t = 80$ proceeds relatively rapidly compared to the subsequent evolution due to diffusion of momentum. The dotted curve shows the profile at $t = 160$, and it is evident that the viscous evolution of the laminar flow is on a relatively slow time scale compared to the more rapid mixing phase that preceded it.

The nearly linear part of the profile at $t = 80$, seen in figure 5(*a*), extending from about $r = 0.5$ to $r = 1.5$ is interesting. It is not solid-body rotation, which would require $\bar{v} \propto r$. Figure 5(*b*) shows that the instability has caused a redistribution of the initial absolute angular momentum, $L = Vr + \frac{1}{2}fr^2$, that extends well beyond the instability region. It is seen that $|L|$ has greatly been reduced within the vortex.

For the anticyclone, the Rayleigh discriminant (1.2) Φ is negative where L (1.3) is negative and $Q = (1/r)\mathrm{d}L/\mathrm{d}r$ is positive. Mixing angular momentum L will tend to make it more uniform and hence decrease Φ. The instability reduces Φ in the region where it was originally negative by decreasing the magnitude of both L and Q. As can be inferred from figure 5(*b*), even at $t = 160\Phi$ is still negative in a range that encompasses the original instability range, although much reduced in magnitude. The total amount of energy lost between $t = 0$ and $t = 80$ was 20 % of the initial total energy in this case with $N^2 = 2$ and $Re = 10^4$. The non-dimensional time $t = 80$ corresponds to approximately seven days at the pole and somewhat longer at mid-latitudes.

4.2. *Density mixing and internal wave radiation*

The instability also strongly perturbs the density. In figure 6 we show the evolution of the isopycnals. The times of the panels are the same as in the sequence showing v in figure 4. At $t = 20$ and $t = 25$ (figures 6*b* and 6*c*) we see overturns that are due to the action of the strong dipolar vortices seen in figures 3(*c*) and 3(*d*). The overturns result in gravitational instability, producing mixed regions of low stratification as seen

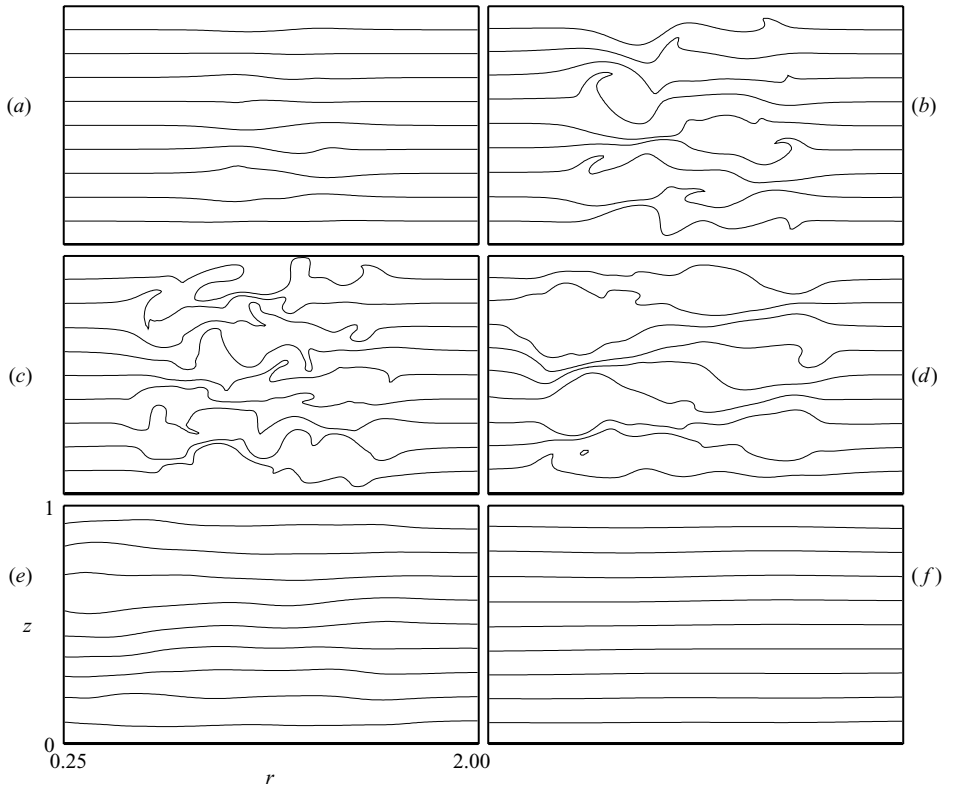

FIGURE 6. Snapshots of the isopycnals taken at the same times and covering the same portion of the domain as in the plots of velocity contours shown in figure 4. ($Re = 10^4$, $N^2 = 2$).

at $t = 35$ (figure 6*d*). Also there are thin regions of intense stratification separating the regions of low stratification as has been observed in earlier studies (cf. Carnevale, Briscolini & Orlandi 2001). When the vortex has substantially relaxed ($t = 80$), the isopycnals are again mainly horizontal. We calculated the vertically averaged value of N taken as a function of r to estimate the amount of mixing that has occurred. At $t = 80$, this averaged value is about 2 % less than the far-field value. This change is relatively small given that during the more vigorous phases of the evolution, the local value of N fluctuates by as much as 50 % over large regions. Over the course of the simulation the maximum perturbation potential energy remains small, reaching at most 0.6 % of the total energy.

During the instability, energy may be lost through internal wave radiation. To measure the amount of energy lost, we added a sponge layer and kept track of the amount of energy absorbed there. This layer extends from from $r = 10$ to $r = 15$. In that region, and only in that region, the waves were damped by a Rayleigh friction, that is a damping of the velocity and density perturbations at a rate proportional to their amplitudes. The coefficient of proportionality was adjusted so that the damping was strong enough to absorb the internal waves before they reached the sidewall at $r = 15$, and small enough to avoid any reflections at $r = 10$. The frequency spectra of perturbations at radial positions outside the vortex, beyond $r = 3$, showed that the frequencies lie within the range from f to N as is expected from linear internal wave theory. For the case with $N = f$, we found essentially no oscillations in the far field

as expected, since when $N = f$ the system cannot support freely propagating internal waves. We found that the amount of energy lost via internal wave radiation in the $N^2 = 2$ case is less than 1/100 of a percent of the total energy loss. For larger values of N^2 the relative loss is even smaller than this. Thus, it seems that pure inertial instability leads to very little internal wave radiation. Larger amounts of internal wave energy may be generated if the constraint of circular symmetry is relaxed. In Carnevale *et al.* (1997) we did find some evidence for this but did not study it in detail. Further computational effort (with fully three-dimensional simulations) will be required to establish whether significant amounts of internal wave energy can be emitted by inertially unstable vortices if they are allowed to develop freely.

5. Anticyclones for a range of Re and N

The example presented above is one of a large set of more than a thousand simulations that we have performed to systematically study the effect of variation of both N and Re on the inertial instability. In what follows, we will first present our results for the anticyclone with $\alpha = 3$, $Ro = -1$.

5.1. *Vertical scale selection and growth rates*

As mentioned in § 2, increasing N is expected to decreases the vertical wavelength of the instability. This is illustrated in figure 7. Comparing panels (*a*) with (*b*), or (*c*) with (*d*), we see that increasing N results in flatter rib vortices. Comparing (*a*) with (*c*) or (*b*) with (*d*), we see that increasing Re also results in flatter rib vortices. The part of the computational domain shown in these panels has dimensions 1×1. Here again the aspect ratio of the structures in the figure is the physical aspect ratio.

To make a quantitative comparison of dominant vertical scales for different N and Re, for each simulation we determined the radial position r where the vertically averaged ω_θ^2 was maximal and then calculated the Fourier sine transform $F(m)$ of ω_θ with respect to z at that radial position. The vertical wavenumber representative of the disturbance was then calculated as the mean of the vertical wavenumber weighted by the vertical wavenumber spectrum:

$$m \equiv \frac{\sum m' F(m')^2}{\sum F(m')^2}, \tag{5.1}$$

where the sums run from $m' = 1$ (representing the largest vertical mode) to $m' = M - 1$ where M is the number of gridpoints in the vertical direction. A plot of m measured in this way, in the early stages of the evolution, is shown as a function of Re in figure 8(*a*) and as a function of N^2 in figure 8(*b*). The analysis was performed at time $t = 5$ because for all of the simulations involved, this time was in the exponential phase of the growth of meridional kinetic energy. Both panels show monotonic growth of m with N^2 and Re, respectively; m behaves as $m \propto N^{1/5}$ for the high values of N and $Re^{1/3}$ for the high values of Re. These power laws are drawn with thick solid lines in the corresponding panels. The 'best-fit' between prosed parameterized curves and data here and elswhere in the paper is obtained using the standard 'gnuplot' algorithm.

During the early phase of the instability, as the rib vortices are growing in amplitude but are not yet strong enough to begin forming dipolar structures, the meridional energy associated with the motion in the (r, z)-plane grows exponentially.

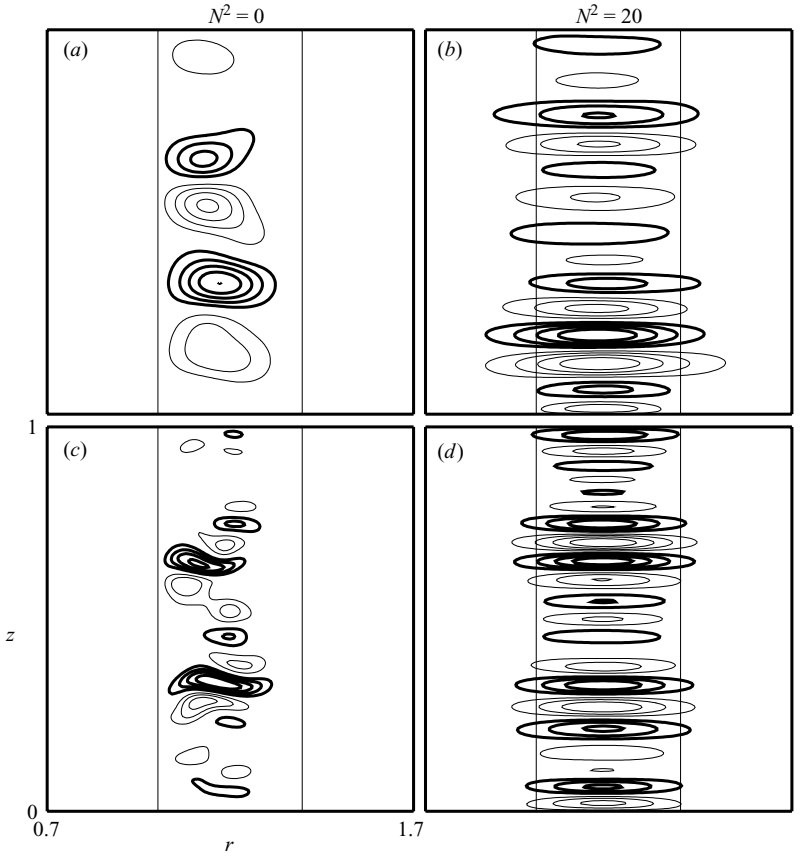

FIGURE 7. Contours of the vorticity ω_θ in a vertical cross-section during a very early phase in the evolution ($t = 10$). These graphs illustrate the role the Reynolds number and N^2 play in the selection of the dominant vertical wavelength of the instability. $\Delta\omega_\theta$ is the contour interval used in each frame. (*a*) $N^2 = 0$, $Re = 5 \times 10^3$, $\Delta\omega_\theta = 0.1$. (*b*) $N^2 = 20$, $Re = 5 \times 10^3$, $\Delta\omega_\theta = 0.01$. (*c*) $N^2 = 0$, $Re = 20 \times 10^3$, $\Delta\omega_\theta = 0.7$. (*d*) $N^2 = 20$, $Re = 20 \times 10^3$, $\Delta\omega_\theta = 0.05$.

The meridional energy in the axisymmetric flow can be written as

$$K = \frac{1}{2}\iint \rho_0(u^2 + w^2) r \, \mathrm{d}r \, \mathrm{d}z.$$

For the simulations that we performed with various values of N and Re, the meridional energy always showed a period of exponential growth and the time $t = 5$ fell in that range. To give an estimate of γ, the growth rate for the instability, or more specifically the growth rate for the amplitude of the meridional velocity field, we calculated

$$\gamma = \frac{1}{2}\frac{1}{K}\frac{\mathrm{d}K}{\mathrm{d}t} \tag{5.2}$$

at time $t = 5$. The factor of $\frac{1}{2}$ takes into account that the velocity enters K quadratically.

As seen above (figure 8*a*) the vertical scale of the instability decreases with increasing N, suggesting that viscosity will act more efficiently. This competes with the inviscid tendency of the smaller scales to grow more rapidly. The net effect is found to be that for increasing N the growth rates decrease (figure 9*a*) according to $\gamma = \gamma_0(1 - N/N_c)$

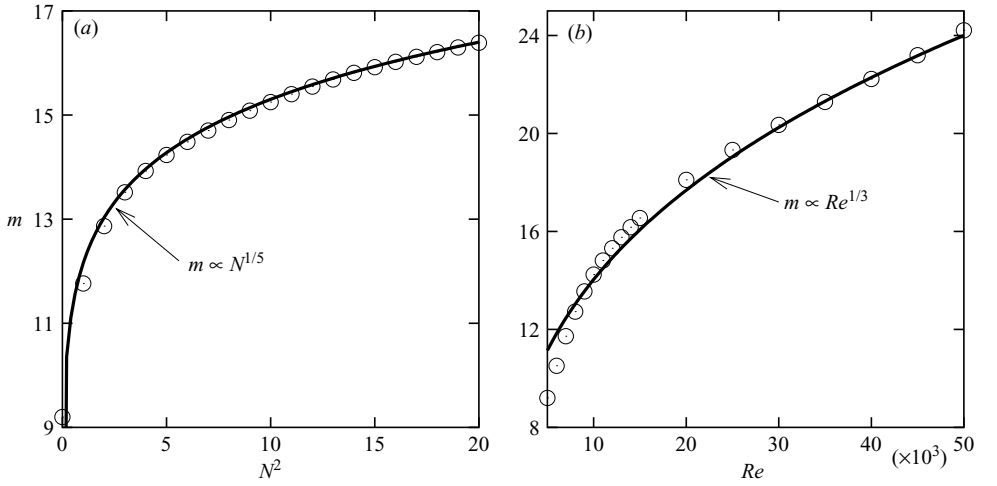

FIGURE 8. Vertical wavenumber m of the instability as a function of (*a*) N^2 with fixed $Re = 10^4$ and (*b*) Re with fixed $N^2 = 5$. In each panel, the data (marked by ○) is taken at time $t = 5$ which is during the early part of the exponential growth phase of the meridional energy. Also shown (thick solid lines) are power-law curves that approximately fit the data.

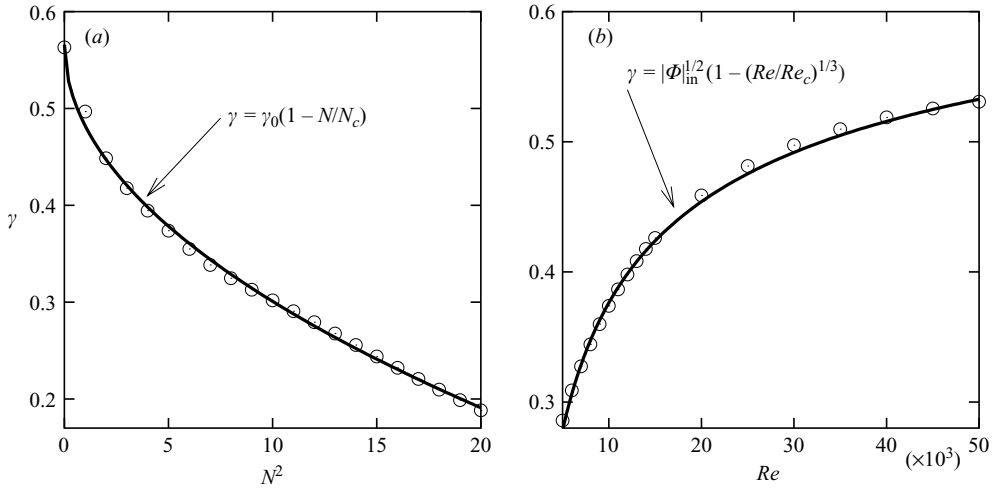

FIGURE 9. The growth rate γ of the meridional energy, measured during the nearly exponential growth phase of the meridional energy. (*a*) The growth rate as a function of N^2 with $Re = 10^4$ from simulations (data points) with a fit to the function $\gamma = \gamma_0(1 - N/N_c)$ ($\gamma_0 = 0.56$ is fixed to match the data point at $N = 0$, and then choice $N_c = 6.8$ gives the best overall fit between the data points and the function.) (*b*) The growth rate as a function of Re with $N^2 = 5$ with a fit to the function $\gamma = |\Phi|_m(1 - (Re/Re_c)^{-1/3})$ (where $|\Phi|_m = 0.75$ is the theoretical upper limit and $Re_c = 1.3 \times 10^3$ is chosen for the best overall fit).

where γ_0 is the growth rate for $N = 0$, and N_c is the critical point where N is too large to permit growth for the given Re. Both of these parameters are functions of Re. On the other hand, for fixed N, increasing Re allows the growth of shorter-wavelength modes which, in accord with inviscid theory, have higher growth rates (figure 9*b*). Note that in both panels γ is below the inviscid maximum growth rate $|\Phi|_m^{1/2} = 0.75$. Comparing figure 8(*b*) with 9(*b*), we see that as Re is increased the vertical wavenumber of the

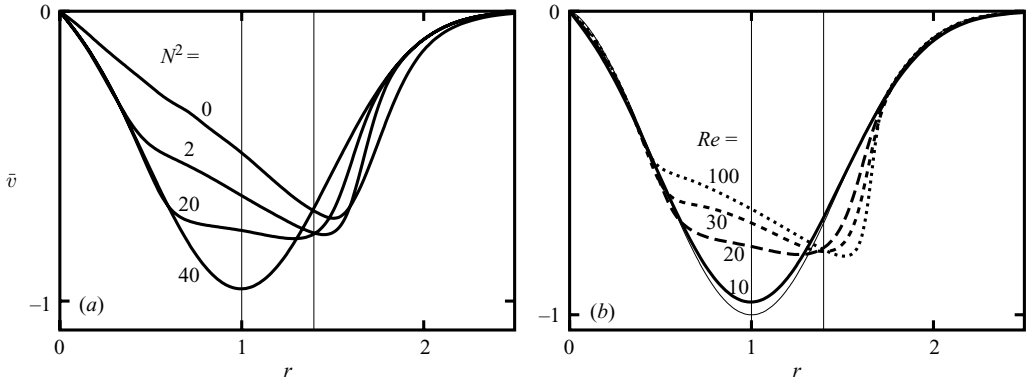

FIGURE 10. (*a*) The vertically averaged swirl velocity $\bar{v}(r,t) = \int_0^1 v(r,z,t)\,\mathrm{d}z$ shown at times when most of the meridional motion has ceased and the vortex has reached a quasi-steady state. For $N = 0$ angular momentum mixing leads to solid-body rotation in the core of the vortex. For $N = 0$ the curve is at time $t = 200$, for all other cases $t = 80$. For $N^2 = 40$, except for the effects of slow viscous diffusion, the profile has barely changed from the initial $\alpha = 3$ profile. In each case shown $Re = 10^4$. (*b*) $\bar{v}(r,t)$ at time $t = 80$ for $N^2 = 40$ with $Re = 10^4$ (thick solid), 20×10^3 (long dash), 30×10^3 (dash), 10^5 (short dash). The initial condition is also shown (thin solid).

instability increases and so does the corresponding growth rate γ. For ever higher Reynolds number we should expect that γ continues to increase, but as we showed in § 2 it can never exceed the upper bound $|\Phi|_{\mathrm{m}}^{1/2}$. With this in mind, the data were compared to the formula $\gamma = |\Phi|_{\mathrm{m}}^{1/2}(1 - (Re/Re_{\mathrm{c}})^{-\xi})$. An excellent fit was found with exponent $\xi = 1/3$ and Re_{c} (the critical Re for a given N^2) $= 1.3 \times 10^3$.

5.2. *Reformation of the anticyclone*

The extent to which the vortex velocity profile is changed by the instability for various values of N is shown in figure 10(*a*). For very small N, redistribution of angular momentum occurs all the way to the centre of the primary vortex ($r = 0$). This results in a velocity profile that has solid-body rotation in the core. For increasing N, the range over which the velocity distribution is altered is ever smaller. In each case, for $N \lesssim 20$, the final structure of the vortex includes a range in which the velocity $\bar{v}(r)$ appears to have a linear dependence on r and the peak velocity has shifted to larger r outside the original instability region. In the case of $N^2 = 40$, the velocity profile is essentially unchanged for this relatively low Reynolds number $Re = 10^4$. The instability with $N = 0$ proceeds with the formation of stronger rib vortices than for higher values of N. The instability is also more vigorous the higher the Reynolds number. Thus we are led to speculate that in the limit of $Re \to \infty$ the result of the instability would be solid-body rotation in the core independent of the value of N. We thus ask whether the result of instability would be closer to solid-body rotation for any value of N for a higher Re. In figure 10(*b*) we show the equilibrated velocity profiles as a function of Re for a fixed value of $N^2 = 40$. It is seen that the effect of increasing Re is to bring the curves closer to solid-body rotation in the core of the vortex. Also note that the slope with which the curve transitions from the new peak back to the initial curve at large r increases with Re, suggesting an almost discontinuous transition for very high Re.

The solid-body rotation that is approached in the limit of high Reynolds number is $-(f/2)r$ in the core. This implies that the absolute angular momentum $\bar{L}$ approaches

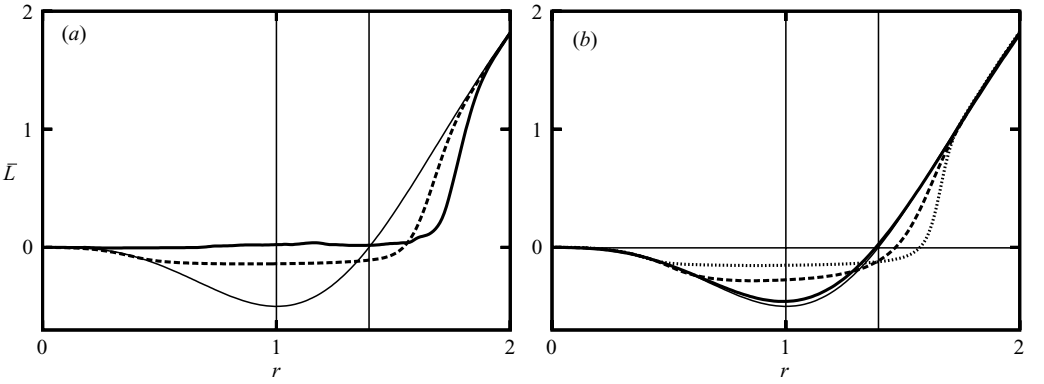

FIGURE 11. (*a*) Absolute angular momentum $\bar{L} = \bar{v}r + \frac{1}{2}fr^2$ at time $t = 200$ for $N^2 = 0$ (thick solid) and $N^2 = 5$ (dashed) with $Re = 50 \times 10^3$. The initial state is also shown (thin solid). The initial inviscid instability region is between the vertical lines. (*b*) $\bar{L}$ at time $t = 80$ for $N^2 = 40$ with $Re = 10^4$ (thick solid), 20×10^3 (dashed) and 10^5 (dotted). The initial condition is also shown (thin solid). The $\bar{L}$-distributions in (*b*) correspond to the $\bar{v}$ profiles shown in figure 10(*b*) but with the $Re = 30 \times 10^3$ case left out.

zero there. This is clearly seen in figure 11. Panel (*a*) shows that for fixed high *Re*, with decreasing *N*, $\bar{L}$ approaches zero from $r = 0$ to beyond the outer edge of the original instability region. Panel (*b*) shows the same tendency when *N* is held fixed while *Re* increased.

Figure 11 shows that for finite *Re*, in the equilibrated states Φ may still negative, that is, in a range where $\bar{L} < 0$ we still have $\bar{Q} = (1/r)\mathrm{d}\bar{L}/\mathrm{d}r > 0$. Both are greatly diminished in amplitude however so that $|\Phi|_\mathrm{m}$ has been reduced to much smaller values than initially. So, inviscidly these flows would be unstable but no further inertial instability ensues because viscous damping can overwhelm any inviscid instability growth if *Re* is sufficiently small.

Analogous results have been found by Griffiths (2003*a*, *b*) for a barotropic parallel shear flow on the equatorial β-plane. There the criterion for instability is that $fQ < 0$ and 'neutralization' of the flow is effected by the inertial instability by creating a region with $f\bar{Q} \approx 0$ which encompassed the original instability region (see also Shen & Evans 1998). With finite viscosity, slightly negative $f\bar{Q}$ were found but sufficiently small in amplitude for the equilibrated flow to be stable. Griffiths concluded that the instability leads to a homogenization of $\bar{Q} \approx 0$ to set $f\bar{Q} \approx 0$ there while elsewhere $f\bar{Q} > 0$.

Another related study is that of Jacquin & Pantano (2002) where the neutralization of inertially unstable vortices with a superposed axial flow is discussed. There data are shown that indicate that in the unstable region where $\Phi < 0$ originally, the instability changes Φ to $\Phi \approx 0$ and $\Phi > 0$.

5.3. *Infinite-Reynolds-number limit*

Extrapolating from the results presented above, we can now hypothesize what the result of inertial instability is in the limit of infinite Reynolds number. Figure 11(*b*) shows that the trend with increasing *Re* is that the equilibrated angular momentum will be zero from $r = 0$ out to some radius where it will increase rapidly, rejoining the curve that defines the initial absolute angular momentum. The instability mixes positive angular momentum from the region beyond the initially unstable region with negative angular momentum from smaller *r* values to produce zero angular momentum. The steepening of the angular momentum curve, as *Re* increases at

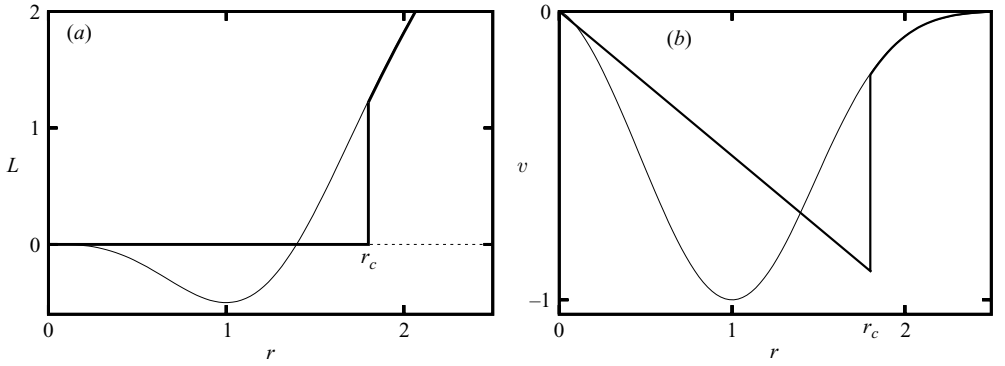

FIGURE 12. (*a*) Construction to determine the new absolute angular momentum L and hence the new azimuthal velocity field that would result due to mixing of momentum for an anticyclone in the limit $Re \to \infty$. The thin curve is the angular momentum of the original $\alpha = 3$ anticyclonic vortex. The thick curve is the proposed re-equilibrated angular momentum. (*b*) The proposed azimuthal velocity field based on the hypothetical equilibrated absolute angular momentum shown in (*a*).

the point where it rejoins the initial curve suggests that, in the limit $Re \to \infty$, the curve will jump from zero to its initial value at some radius r_c. A prediction for the value of r_c can be made on the basis of the construction shown in figure 12. Here r_c is just large enough so that the total absolute angular momentum in the initial profile (thin line) integrated from $r = 0$ to $r = r_c$ is zero. The profile of the proposed equilibrated L-distribution (thick line) would have completely homogenized absolute angular momentum out to r_c, while leaving L beyond r_c unchanged (note that the total angular momentum $\iiint L \mathrm{d}\mathscr{V}$ of the proposed equilibrated velocity profile will equal that of the initial velocity distribution). Thus r_c can be computed from the formula

$$\int_0^{r_c} Lr \,\mathrm{d}r = \int_0^{r_c} (rV(r) + fr^2/2)r \,\mathrm{d}r = 0, \tag{5.3}$$

where $V(r)$ is the initial velocity distribution.

In other words, the evidence presented above indicates that for all values of N, in the infinite-Reynolds-number limit, the instability will completely mix the angular momentum from $r = 0$ out to r_c and will not effect the flow beyond $r = r_c$. The resulting equilibrated velocity profile based on this construction is shown in figure 12(*b*). We have solid-body rotation with $v = -fr/2$ from $r = 0$ to $r = r_c$ and the initial velocity profile beyond. The discontinuity at $r = r_c$ agrees with the extrapolation to high Re expected from figure 10(*b*) for the profile at high but finite values of Re. One might ask why the mixing need extend all the way to the axis ($r = 0$); why could it not stop at some positive value $0 < r < 1$ ($r = 1$ being the lower limit of the unstable region)? This would create a zone where $\mathrm{d}L/\mathrm{d}r > 0$ with $L < 0$ which would be unstable. Thus inertial instability will prevent this from happening and the erosion of the $L < 0$ region will continue down to the only point at which it can terminate without forming such an unstable zone. That point can only be the origin.

One must bear in mind that a sharp gradient in L at r_c can form only in flows where the circular symmetry is maintained. If this is relaxed, that is if θ-variations are allowed, the hypothetical equilibrated profile drawn in figure 12(*b*) and the profiles for example shown in figure 10 are expected to be unstable to perturbations that break the circular symmetry (see Afanasyef & Peltier 1998 and remarks in § 7).

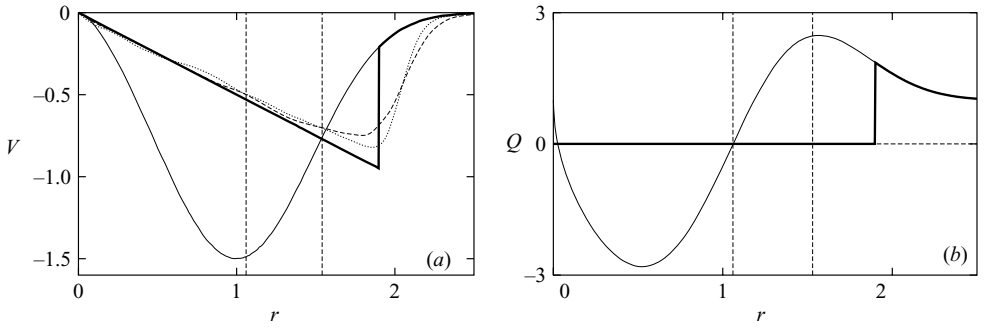

FIGURE 13. Velocity and potential vorticity profiles for an $\alpha = 3$ anticyclone with $Ro = -1.5$ and $N = 0$. (*a*) The velocity profiles V for the initial condition (thin line), the prediction (thick line) and the vertically averaged velocity $\bar{v}$ at $t = 160$ ($Re = 20 \times 10^3$ dashed; $Re = 40 \times 10^3$ dotted). (*b*) The potential vorticity profile Q for the initial condition (thin line) and the prediction (thick line). In each panel, the vertical dashed lines delimit the unstable region, $1.06 < r < 1.54$.

To check that the prediction based on this construction is also valid for high-Rossby-number anticyclones, we performed a series of simulations with increasing Ro and various values of Re. As Ro increases the computational burden also increases because energetic small scales are produced, and thus we cannot easily go to Ro much below -1.5 with our current resources. The case $Ro = -1.5$ (with $N = 0$) is illustrated in figure 13. In panel (*a*), initial and predicted azimuthal velocity profiles are shown, along with the vertically averaged profiles for the cases $Re = 20 \times 10^3$ and $Re = 40 \times 10^3$ at $t = 160$. Qualitatively, the large drop in magnitude of the velocity at its peak, the shift in the peak to larger r and the relative steepness of the curves for r beyond the peak suggest that the prediction is capturing the correct tendency. Comparison of the two cases shows that with increasing Re, the velocity minimum and the steepness of the profile tend toward the predicted values.

We expect that the theoretical construction can be applied to any anticyclone that has an initial L-distribution qualitatively similar to that shown in figure 2(*b*) or figure 12(*a*), that is, an L-distribution with $L < 0$ for some finite range starting at the centre $r = 0$ and with $L > 0$ and monotonically increasing for larger r. To check this, we have also performed a series of simulations for the $\alpha = 2$ case and found that there too, for high Reynolds numbers, solid-body rotation was attained in the core of the equilibrated vortex (see figure 27 below for an example). Additionally, unstable anticyclonic vortices with a Gaussian vorticity distribution (the so-called Lamb–Oseen vortex) were also tested. Although these are non-isolated vortices, their angular momentum distribution is qualitatively similar to the isolated anticyclones tested above. The redistribution of angular momentum proceeds in a manner completely analogous to that in unstable isolated anticyclones. Thus the proposed construction for the redistribution of angular momentum in the $Re \to \infty$ case also applies to unstable non-isolated anticyclones.

The concept of angular momentum mixing underpins the construction that we have given here. The construction predicts $Q = 0$ in the region of uniform L ($r < r_c$). For $r > r_c$ we have

$$\int_0^{r>r_c} Qr \, \mathrm{d}r = L(r > r_c)$$

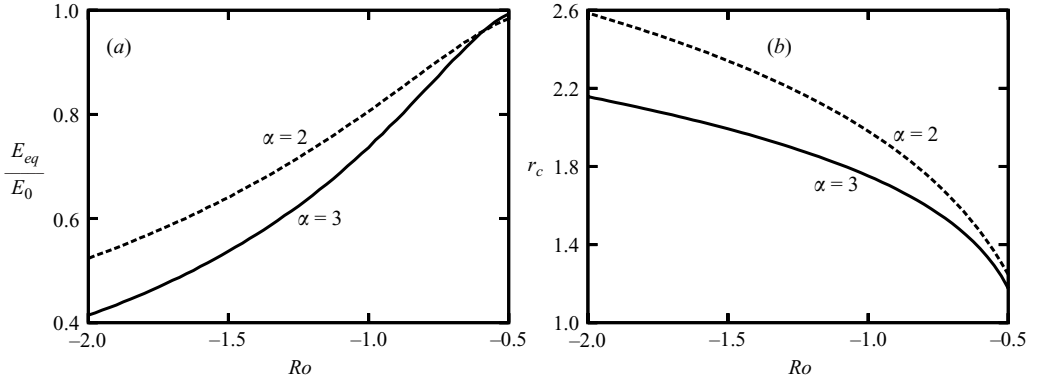

FIGURE 14. (*a*) The ratio of final equilibrated E_{eq} energy to initial energy E_0 for the hypothetical transition of an unstable anticyclonic vortex to the final stable vortex due to mixing of angular momentum. Two cases are shown: $\alpha = 2$ (dashed line) and $\alpha = 3$ (solid line). (*b*) The position r_c of the peak velocity in the proposed equilibrated azimuthal velocity for an initial profile with $\alpha = 2$ (dashed line) and $\alpha = 3$ (solid line).

which implies that total Q is conserved because for $r > r_c$, L is unchanged. Hence, one could interpret the 'neutralization' of the flow by inertial instability to be due to potential vorticity mixing while preserving total potential vorticity. But this is insufficient to predict the equilibrated state without also considering the absolute angular momentum mixing subject to conservation of total angular momentum. For example, consider the potential vorticity distribution for the $Ro = -1.5$ case shown in figure 13(*b*). The two vertical lines mark the end points, r_0 and r_1, of the unstable region (where $L < 0$ and $Q > 0$). If we consider just mixing Q from the region where it is negative with that in the region where it is positive, in a way that conserves the total $Q_{\text{tot}} = \int Q r \mathrm{d}r$, the predicted end point of the mixed region would coincide with r_1 the right-hand end of the unstable region, because there $L(r_1) = 0$ and $\int_0^{r_1} Q r \mathrm{d}r = L(r_1)$ Then the presumed equilibrated velocity profile would be solid-body rotation, $\bar{v} = -\frac{1}{2} f r$ between $r = 0$ and $r = r_1 < r_c$, which is continued for $r > r_1$ by the original velocity profile. Now since $\bar{v} < V$ for $r < r_1$ and $\bar{v} = V$ for $r > r_1$, one sees that total L would not be conserved (the hypothetical total L would have decreased). So, how can total Q be conserved in our prediction while also preserving total L? In this regard figure 13(*b*) is not complete. With $Q = 0$ between $r = 0$ and $r = r_c$, total Q would appear not to be conserved; in fact it would appear to have decreased. So some positive Q appears unaccounted for. But as figure 13(*a*) indicates, for finite Re the equilibrated profile has an associated Q that takes very large positive values in a narrow region for $r > r_c$. In our infinite-Reynolds-number limit, this mathematically reduces to a δ-function behaviour at $r = r_c$ which accounts for the 'missing' positive Q.

With the hypothesized infinite-Reynolds-number profile, we can now predict how much kinetic energy is lost in the mixing process. The theoretical ratio of the kinetic energy in the final equilibrated vortex E_{eq} to the initial energy E_0 is shown in figure 14(*a*) for both $\alpha = 2$ and $\alpha = 3$ initial vortices. We see that the more negative the Rossby number, the more energy is lost during the equilibration. With Ro near the marginally unstable values (for $\alpha = 3$, $Ro_c \approx -0.39$; for $\alpha = 2$, $Ro_c \approx -0.30$) little energy is lost, while losses near 50 % result if $Ro = -2$. Also we note that for most of the range shown, more energy is lost in the equilibration of $\alpha = 3$ vortices than for $\alpha = 2$ vortices.

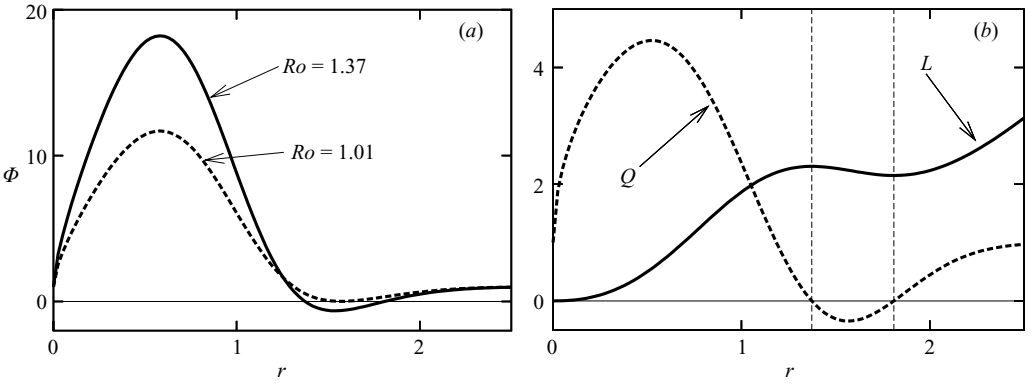

FIGURE 15. (*a*) The Rayleigh discriminant Φ for the case of a cyclone with $\alpha = 3$ for $Ro = 1.01$ and $Ro = 1.37$. (*b*) The absolute angular momentum L (solid line) and absolute vorticity Q (dashed line) for the case $\alpha = 3$ and $Ro = 1.37$. The Rayleigh discriminant $\Phi = (2L/r^2)Q \leqslant 0$ for the range of r-values indicated by vertical dashed lines (between $r \approx 1.37$ and $r \approx 1.81$). In this range $L > 0$ and $Q \leqslant 0$. The minimum value of Φ is -0.645 and thus $|\Phi|_{\mathrm{m}}^{1/2} = 0.80$ (the upper limit for the inviscid growth rate).

For $\alpha = 3$ and $Ro = -1.5$, the prediction from figure 14(*a*) is a loss of 46 %. The equilibrated flows for this case shown in figure 13(*a*) have at $Re = 20 \times 10^3$ a 57 % loss, and at $Re = 40 \times 10^3$ a 53 % loss.

Assuming that our hypothesis is correct for any Rossby number, a simple calculation shows that for large $|Ro|$, $E_{eq}/E_0 \propto 1/|Ro|$, not unlike the trend already seen in figure 14(*a*) for still relatively small $|Ro|$.

6. Cyclones for a range of *Re* and *N*

We next examine the effect of inertial instability on cyclones. We chose for the initial cyclone the same velocity profile as used in the anticyclonic case, that is, the $\alpha = 3$ velocity profile but with $U > 0$ (see (3.1)). Furthermore, we chose the amplitude U of the cyclone to be such that the ensuing instability has growth rate γ comparable to that in our $Ro = -1$ anticyclonic example (with $N = 0$ and $Re = 10 \times 10^3$). For this we found that $U = 1.37$, that is $Ro = 1.37$ was a good choice. The Rayleigh discriminant for the cyclone is plotted in figure 15(*a*) for $Ro = 1.37$ as well as that for the marginal case $Ro = 1.01$. Φ is negative in the $Ro = 1.37$ case in the range $1.37 \lesssim r \lesssim 1.82$ where $Q < 0$ (see figure 15*b*). The width of the instability region is comparable to that in the anticyclone example with $Ro = -1$ (see figure 2 or figure 5) and the maximum speed in the instability range is about 1, which was also the maximum speed in the instability range for the anticyclone.

6.1. *Vertical scale selection and growth rates*

In figure 16(*a*) we compare the variation of the vertical wavenumber of the instability in the cyclone case (solid line) and the anticyclone case (dashed line). The choice $Ro = 1.37$ for the cyclone produces a growth curve that matches well the corresponding curve for the anticyclone with $Ro = -1$, not only at $N = 0$, but also over the whole range shown. Comparing the graphs for the variation of the growth rate as Re is varied in figure 16(*b*) shows also that they are very similar for both cyclones and anticyclones. The point at which the curves intersect depends on the choice of Ro

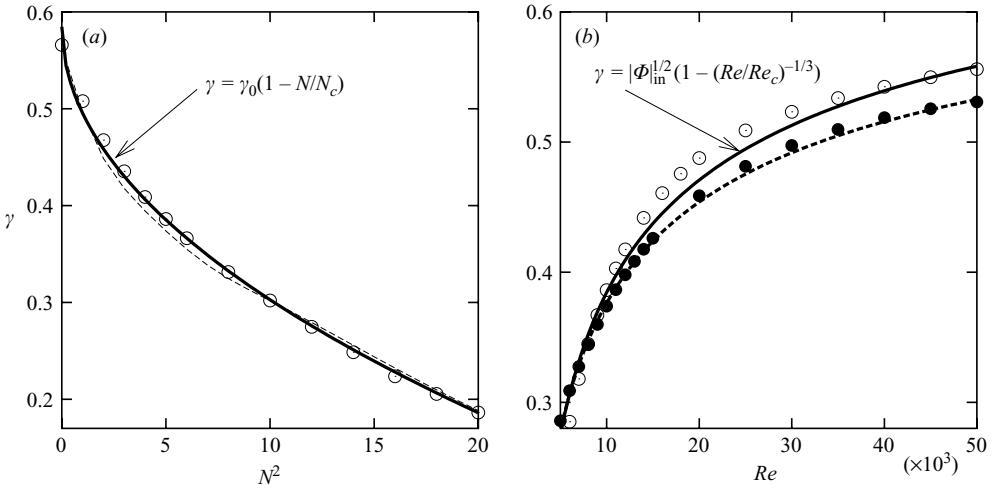

FIGURE 16. The maximum (exponential) growth rate γ of the meridional energy, during the nearly exponential phase of meridional energy growth for a cyclone with $Ro = 1.37$. (*a*) The growth rate as a function of N^2 with $Re = 10^4$ from simulations (data points) with a fit to the function $\gamma = \gamma_0(1 - N/N_c)$ (where $\gamma_0 = 0.58$ is chosen to match the the data point at $N = 0$ and $N_c = 6.6$ is then chosen to give the best overall fit to the data). The dashed line is a line passing through the corresponding data points in the anticyclonic case shown in figure 9(*a*). (*b*) The growth rate (open circles) as a function of Re with $N^2 = 5$ with a fit to the function $\gamma = |\Phi|_{\rm m}^{1/2}(1 - (Re/Re_{\rm c})^{-1/3})$ (solid line) (where $|\Phi|_{\rm m}^{1/2} = 0.80$, the theoretical maximum inviscid growth rate and $Re_{\rm c} = 1.4 \times 10^3$) for the case $Ro = 1.37$. For comparison, the data (filled circles) and the corresponding fit (dashed line) are given for the anticyclonic $Ro = -1$ case as previously shown in figure 9(*b*).

for the cyclones, and a better overall match for the curves in figure 16(*b*) could be attained by decreasing the value of Ro for the cyclone, but this would then make the fit in 16(*a*) worse. There is also a good degree of similarity in how the most unstable wavenumber varies with Re and N for the cyclone and anticyclone. In figure 17(*a*), we see that the overall trend for the variation of m with N is the same in both cases, that is higher N results in higher m, although the slope of the curve is somewhat lower in the cyclone case. The quantitative difference is at most about 3 over the range of N investigated (corresponding to a difference of three rib vortices). For the variation of m with Re shown (figure 17*b*), both qualitatively and quantitatively the cyclone and anticyclone cases are very similar.

In studies of stratified Taylor–Couette flow (Hua, Le Gentil & Orlandi 1997*a*) and horizontally sheared equatorial β-plane flow (Griffiths 2003*a*) the vertical wavenumber m of the most unstable mode is found to scale asymptotically with $N^{1/3}$ and $Re^{1/3}$ for large Re in each case. Laboratory experiments with a homogeneous fluid ($N = 0$) by Afanasyev & Peltier (1998) on the other hand suggest a scaling with $Re^{1/2}$ but the Reynolds number in those experiments did not exceed the modest value of 2500. Our 'measurements' shown in figures 8 and 17 were found to be best approximated for the anticyclone by $m \propto N^{1/5}$ and $Re^{1/3}$ but for the cyclone by $m \propto N^{1/8}$ and $Re^{3/8}$, respectively.

The analysis of Griffiths (2003*a*) further suggests that the growth rate of the fastest growing vertical modes may to leading order be $\gamma = |\Phi|_{\rm m}^{1/2}(1 - \text{constant} \times N^{2/3}Re^{-1/3})$ for small N^2/Re. Obviously this cannot be correct when $N = 0$ since, for finite Re,

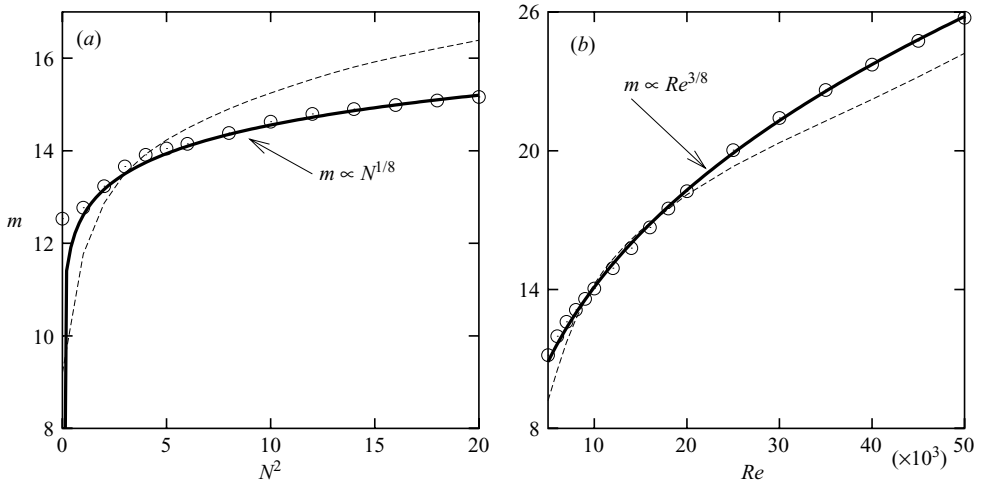

FIGURE 17. Vertical wavenumber m of the instability for a cyclone with $Ro = 1.37$ as a function of (*a*) N^2 with $Re = 10^4$ and (*b*) Re with $N^2 = 5$. In each panel, the data (marked by ○) are taken at time $t = 5$ which is during the early part of the exponential growth phase of the meridional energy. Also shown (thick solid lines) are power-law curves that approximately fit the data. The dashed lines are curves through the corresponding anticyclone data with $Ro = -1$ previously shown in figure 8.

the growth rate will depend on Re and be less than $|\Phi|_{\mathrm{m}}^{1/2}$. This inconsistency seems to be due the hydrostatic approximation made by Griffiths. Figures 9(*a*) and 16(*a*) suggest that for our vortices the correction for $N \neq 0$ to the growth rates found with $N = 0$ at fixed Re are proportional to N for both anticyclones and cyclones. Further, the corrections to the maximum growth rate $\gamma_\infty = |\Phi|_{\mathrm{m}}^{1/2}$ for finite Re seem to be of order $Re^{-1/3}$ for both the anticyclone (figure 9*b*) and the cyclone.

Any discrepancies between these empirically observed scalings here and for example the scalings predicted by the analytical work by Griffiths (2003*a*) may be due to the fact that our experiments were limited to rather small Re and N values. On the other hand, that analytical work pertained to a parallel shear flow on the equatorial β-plane (without horizontal diffusion and with the hydrostatic approximation) and there is no reason to assume that those results should apply to our observations. It is difficult to judge at this point whether our empirical scalings will hold over much larger ranges of N and Re and whether one should expect the scaling to be the same for the cyclone and anticyclone.

6.2. *Re-formation of the cyclone*

Given that the size of the instability region, and the variation of the vertical scale m and the growth rate of the instability are similar for both the $Ro \approx 1.4$ cyclone and the $Ro = -1$ anticyclone, one might expect that the unfolding of the instability for both would be alike. This is further suggested by the contour plots of the evolution of ω_θ in figure 18. Not only are there again dipolar structures that behave similarly to those in the anticyclonic example (figure 3), but the peak values of ω_θ are comparable.

In view of these favourable comparisons, one might expect that the effects of the instability on the primary vortex would be similar. This is not the case. The final equilibrated cyclones are very different from the equilibrated anticyclones. This can best be demonstrated by showing how the velocity profile is changed by the instability. In figure 19(*a*), the initial velocity profile is shown as a thin curve and the

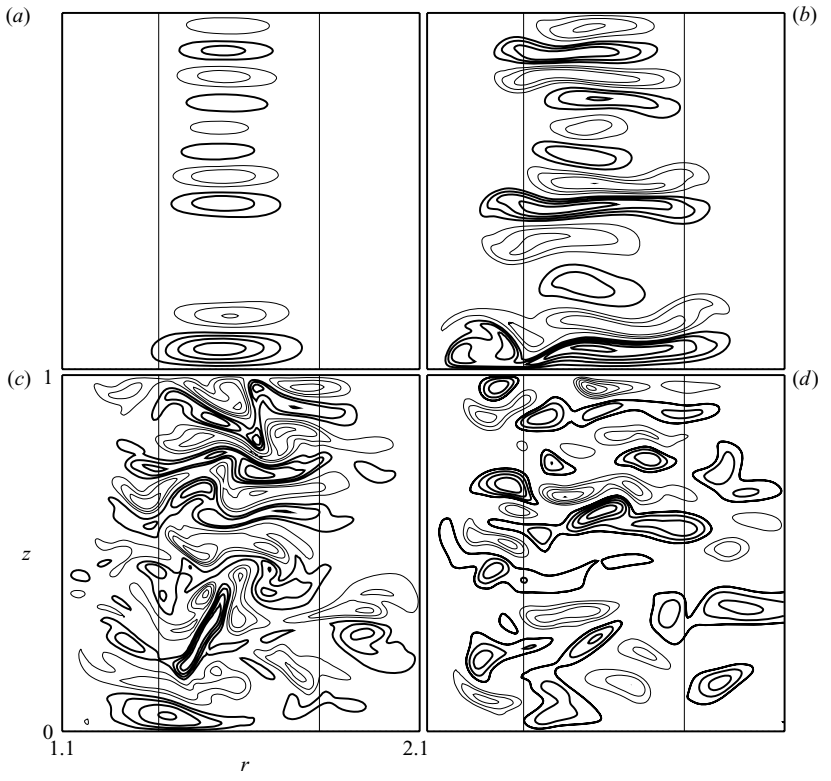

FIGURE 18. Evolution of ω_θ in a vertical cross-section for the cyclone with $\alpha = 3$, $Ro = 1.4$, $N^2 = 2$ and $Re = 10^4$. Thick/thin lines are used for $+/-$ contours. The alternating sign of ω_θ indicates the alternating sense of rotation of the rib vortices that initially start in the unstable region (between the solid vertical lines). The times are (*a*) $t = 10$, (*b*) $t = 15$, (*c*) $t = 20$ and (*d*) $t = 25$. Only a portion of the computational domain is shown. The contour intervals $\Delta\omega_\theta$ for each panel are: (*a*) 0.4, (*b*) 1.4, (*c*) 1.1 (*d*) 0.4. Pairing of rib vortices leads to propagating 'dipoles' which mix angular momentum both inside and outside the initial instability region. Notice the similarities in the evolution with that of the corresponding anticyclonic case shown in figure 3.

thick curves give the equilibrated profiles for two different values of Re (with $N^2 = 5$). In contrast to the anticyclonic case (see for example figure 10), there is very little change in the profile apart from the overall decay in the low Reynolds number case ($Re = 10 \times 10^3$). The main effect of the instability in the higher $Re = 50 \times 10^3$ case is confined in and around the initial instability region where it has only slightly altered the slope of the profile. The instability has not affected the core of the vortex. Since the initial instability regions for both the cyclone and anticyclone in these examples were relatively localized compared to the extent of the change in the cyclonic case, and since in both cases the pairing of the rib vortices permitted the possibility of propagation well beyond the instability region, it may be regarded as surprising that the equilibration is far more localized and subtle in one case (the cyclones) compared to the other (the anticyclones). This difference can be understood in terms of the degree of angular momentum mixing needed to bring the instability to a halt, as discussed further below.

In figure 19(*b*), we compare the equilibrated vortices for two values of N with $Re = 50 \times 10^3$. Again the initial profile is represented by a thin solid line. The $N = 0$

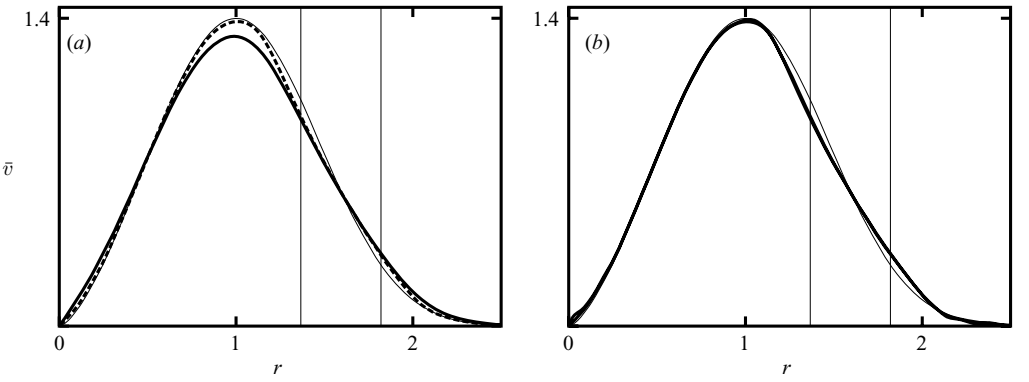

FIGURE 19. (*a*) Vertically averaged swirl velocity $\bar{v}(r, t)$ is shown at time $t = 80$ for the case $N^2 = 5$ with $Re = 10^4$ (thick solid), 50×10^3 (dashed). The initial $\alpha = 3$, $Ro = 1.4$ profile is shown as a thin solid curve. (*b*) $\bar{v}(r, t)$ for the cases $N^2 = 0$ and 50 (thick curves, virtually coincident) with $Re = 50 \times 10^3$ at $t = 80$ (thin curve is the initial condition).

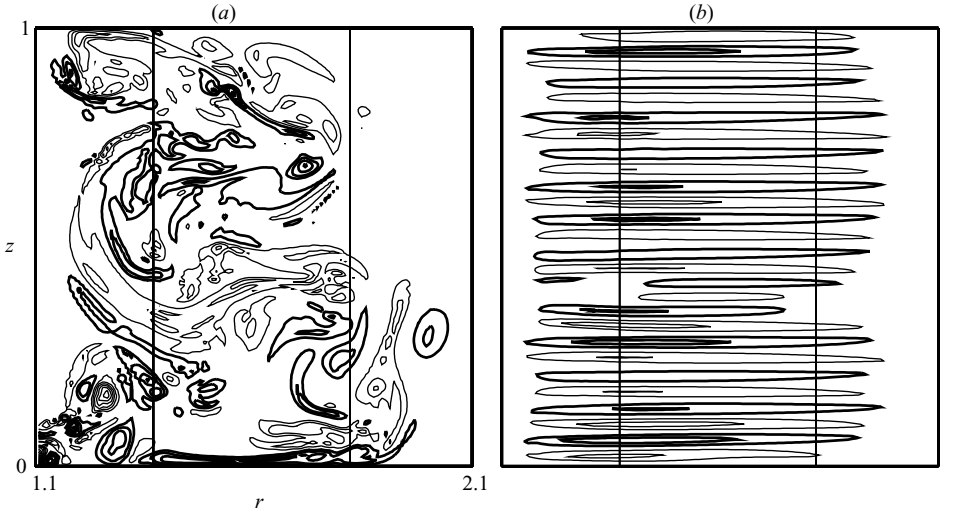

FIGURE 20. ω_θ in a vertical cross-section for the cyclone with $\alpha = 3$, $Ro = 1.4$ for two values of N. In each panel the time was chosen as that for which the maximum value of ω_θ was near its maximum value in time. (*a*) $N^2 = 0$, $t = 15$ (contour interval $\Delta\omega_\theta = 3$), (*b*) $N^2 = 50$, $t = 20$ ($\Delta\omega_\theta = 6$). In both cases $Re = 50 \times 10^3$. Thick/thin lines are used for $+/-$ contours. Only a portion of the computational domain ($0 < r < 4$) is shown.

and $N^2 = 50$ data are both drawn as thick curves but they are almost identical and overlap. As in the $N^2 = 5$ case (panel *a*), there is almost no change from the initial vortex profile except for the small change of slope in and around the initially unstable region. The insensitivity to relatively large variations in N is rather remarkable in the light of figure 20 which shows that the azimuthal vorticity field ω_θ is very different for $N^2 = 0$ and 50. For $N^2 = 0$ (figure 20*a*), the field is very turbulent and disorganized, while for $N^2 = 50$ (figure 20*b*) the field is ordered stack of thin rib vortices oriented only horizontally. Apparently, whether chaotic or not, the evolution proceeds until essentially the same stable state is achieved over a wide range N-values.

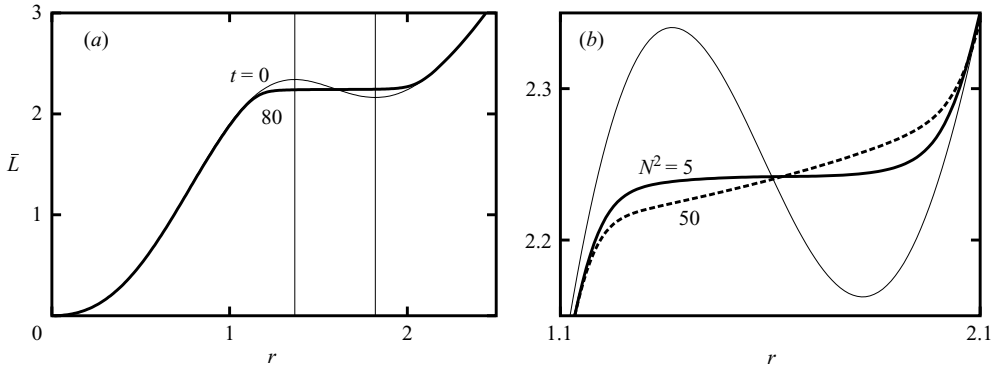

FIGURE 21. (*a*) The angular momentum $\bar{L} = \bar{v}r + \frac{1}{2}fr^2$ for the case $Ro = 1.4$, $N^2 = 5$ with $Re = 50 \times 10^3$ at $t = 80$ (thick solid). The initial condition is also shown (thin solid). Note that the vortex is initially inviscidly unstable where the slope of L is negative (between $r = 1.37$ and $r = 1.82$). (*b*) A close-up view of the angular momentum $\bar{L}$ for the case $N^2 = 5$ (thick solid) as in panel (*a*) and additionally $N^2 = 50$ (dashed) with $Re = 50 \times 10^3$ at $t = 80$.

How can it be that such seemingly similar instabilities, at least at first sight, produce such different results? In both cases, the similarly evolving ω_θ-fields which mix the angular momentum are equally vigorous and extend beyond the initial region of instability. But, in the anticyclonic case, the result is a significant change to the velocity profile extending deep into the originally stable region of the core because the dipolar vortices propagate well away from the instability region towards the centre of the vortex. In the cyclonic case there is only a slight modification of the slope of the velocity profile in a much more limited range, in and around the initial instability region. Here the meridional motions remain confined to a spatially far more limited region.

Some insight can be obtained by examining the evolution of the angular momentum. Figure 21(*a*) shows the initial and equilibrated profile of the angular momentum, with vertical lines marking the boundaries of the instability region in a simulation with $N^2 = 5$ and $Re = 50 \times 10^3$. Since L is positive for all r, for the instability to be complete, at least in the inviscid sense, $\mathrm{d}L/\mathrm{d}r$ must become non-negative everywhere. From the graph of the initial condition, it is seen that this can be accomplished locally by simply mixing the angular momentum from the relative maximum at the left-hand end of the instability region with that from the minimum at the the right-hand end. This seems to be precisely what has happened by time $t = 80$ in figure 21(*a*).

How the equilibrated profiles of angular momentum differ for different values of N is illustrated in figure 21(*b*) where we have enlarged the initial instability region shown in panel (*a*) and added the result for $N^2 = 50$. The lower the value of N, the flatter the curve, in other words the more homogenized or mixed the angular momentum has become. Curiously, the higher the value of N, the more positive the slope of the angular momentum in this region. This could only be achieved by transporting angular momentum from the area near the local minimum to the local maximum and vice versa without thoroughly mixing it, which would have achieved homogenization, that is uniform angular momentum (i.e. $Q = (1/r)\mathrm{d}L/\mathrm{d}r \approx 0$). The more random eddy activities in the low- N case as seen in figure 20(*a*) have mixed more thoroughly than the orderly stack of rib vortices for higher N seen in figure 20(*b*). For a given N, the higher the value of Re, the better should be the mixing and the flatter should be the angular momentum in and around the initially unstable region, and correspondingly

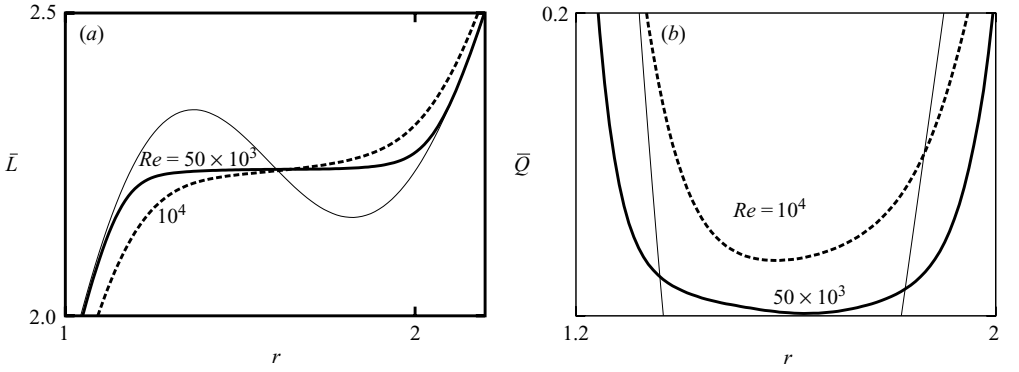

FIGURE 22. (*a*) A close-up view of the angular momentum $\bar{L} = \bar{v}r + \frac{1}{2}fr^2$ for the case $Ro = 1.4$, $N^2 = 5$ with $Re = 50 \times 10^3$ (thick solid) and $Re = 10^4$ (dashed) at $t = 80$. Note that the vortex is initially inviscidly unstable where the slope of L is negative (approximately from $r = 1.37$ to 1.82). (*b*) A close-up view of the potential vorticity $\bar{Q} = \bar{\omega}_z + f = \bar{L}_r/r$ for $N^2 = 5$ with $Re = 50 \times 10^3$ (thick solid) and $Re = 10^4$ (dashed) at $t = 80$. In both panels, the initial condition is also shown (thin solid).

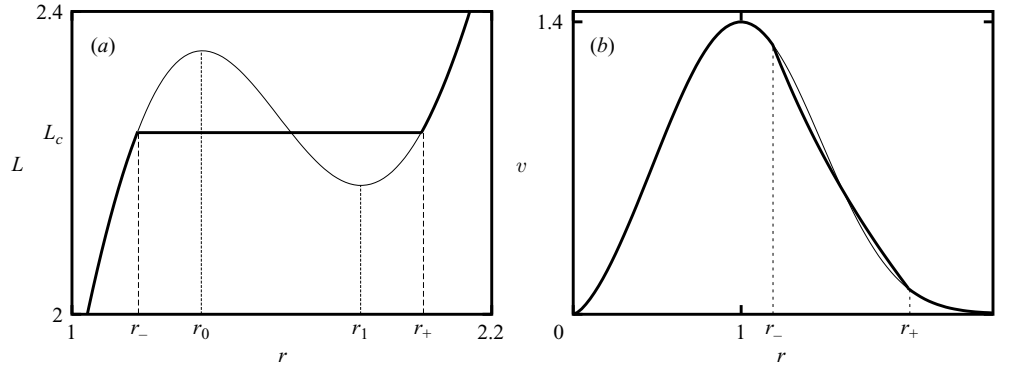

FIGURE 23. (*a*) Construction to determine the new angular momentum and hence the new azimuthal velocity field that would hypothetically result due to mixing of angular momentum for a cyclone. The thin curve is the angular momentum of the original $\alpha = 3$ cyclonic vortex with $Ro = 1.4$. The thick curve is the proposed re-equilibrated angular momentum. r_- and r_+ delimit the region where $Q = 0$ in the equilibrated vortex and r_0 and r_1 delimit the instability region. (*b*) The azimuthal velocity field based on the hypothetical equilibrated angular momentum shown in (*a*).

the lower the value of $|\bar{Q}|$ there. This is confirmed in figure 22 where we show $\bar{L}$ and $\bar{Q}$ for $N^2 = 5$ and $Re = 10 \times 10^3$ and $Re = 50 \times 10^3$.

6.3. *Infinite-Reynolds-number limit*

Based on these results and similar results for other values of Re and N, we arrive at the speculation that as $Re \to \infty$ for any given N, the final angular momentum would be uniform in and around the initially unstable region. Extrapolating from figures 21 and 22, we propose that the equilibrated L for $Re \to \infty$ will be of the form shown in figure 23(*a*). There will be a region of homogeneous, that is constant, L from a point r_- to the left of the initial instability region to r_+ to the right of the initial instability region. This region of constant L is constructed by assuming the total angular momentum is the same before and after the instability. The equation

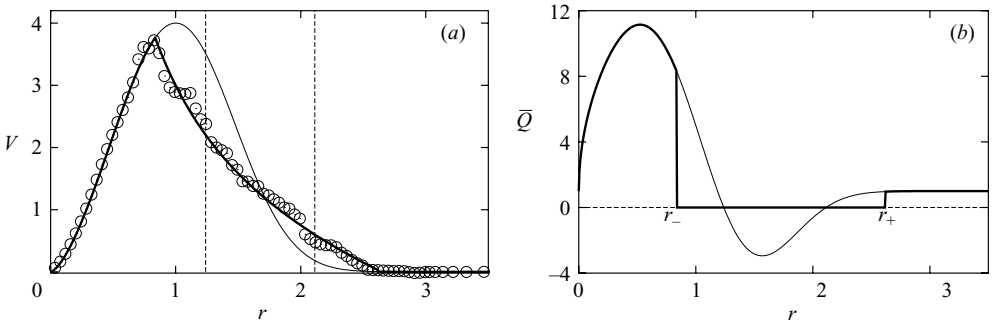

FIGURE 24. Velocity and potential vorticity profiles for a cyclone with $Ro = 4$ and $N = 0$. (*a*) The velocity profiles V for the initial condition (thin line) and the prediction (thick line). The data for the vertically averaged velocity $\bar{v}$ at $t = 5$ ($Re = 25 \times 10^3$) are shown as circles. The vertical dashed lines delimit the unstable region, $1.24 < r < 2.11$. (*b*) The potential vorticity profile for the initial condition (thin line) and the prediction (thick line). The points r_- and r_+ delimit the region of $Q = 0$ predicted by our construction. The unstable region is where $Q < 0$ in the initial profile.

that determines the value of the angular momentum in this region and the positions of its boundaries r_- and r_+ is

$$\int_{r_-}^{r_+} (L - L_c) r \, \mathrm{d}r = 0, \tag{6.1}$$

where $L(r) = V(r)r + \frac{1}{2} f r^2$ and $V(r)$ the initial profile. Equation (6.1) was solved numerically for L_c, r_- and r_+. For a test r_-, there is a corresponding test $L_c = L(r_-)$. The integral is computed using these test values, and if no r_+ could be found for which the integral vanished, another choice was made for r_-. Once L_c, r_- and r_+ are determined the new $L(r)$ is defined, and this is shown as the thick solid line in figure 23(*a*). From this $L(r)$, one then constructs the equilibrated velocity profile from the equation $L(r) = \bar{v}(r)r + \frac{1}{2} f r^2$ (see figure 23*b*). That is, the equilibrated profile will have $\bar{v}(r) = V(r)$ for $0 \leqslant r \leqslant r_-$ and $\bar{v}(r) = V(r)$ for $r \geqslant r_+$ while for $r_- \leqslant r \leqslant r_+$ we have $\bar{v}(r) = L_c/r - \frac{1}{2} f r$. The construction shown in this figure corresponds to the cyclone studied in this section with $\alpha = 3$ and $Ro = 1.4$. The hypothesized profile is very similar to the $Re = 50 \times 10^3$ case shown in figure 19.

Not shown here are how r_- and r_+ vary with the Rossby number. With increasing Ro, r_- shifts further inwards (towards the origin) while r_+ increases. For the $\alpha = 3$ case we find that for $Ro \approx 2.2$, we have $r_- = 1$ so that the equilibrated profile starts at the original position of the peak velocity of $V(r)$. For Ro beyond 2.2, r_- will be to the left of the original peak position, and hence the core of the cyclone will be changed by the instability.

Experiments with $Ro = 3$ and $Ro = 4$ lent further support to our hypothesis: in both cases the peak velocity dropped to smaller values and the peak velocity position is at $r < 1$, at smaller r for $Ro = 4$ than for $Ro = 3$, as predicted by our theoretical construction. A case with $Ro = 4$ is illustrated in figure 24(*a*). There is excellent agreement between the prediction and the simulation. The evolution is very rapid and equilibration towards the predicted form occurs in a relatively short time. The adjustment here is somewhat different from what we observed in the high-Ro anticyclone case discussed above where a long equilibration time was required because

the core equilibrated much more slowly than the region in and around the instability region.

As in the case of the anticyclone, the idea of potential vorticity mixing alone is insufficient to predict the equilibrated state in inertial instability. As for the anticyclone, achieving stability requires creation of a region with $Q=0$ or equivalently uniform L. In figure 24(b), we show the graph for the potential vorticity in the $Ro=4$ cyclonic case, along with two vertical lines that mark the end points, r_- and r_+, of the region where Q has been brought to zero to achieve equilibrium. Note that the instability region is where $Q<0$, and the equilibrated $Q=0$ region extends beyond this on both sides. If we consider just mixing Q, say in a way that conserves the total ($\int Qr\,\mathrm{d}r$), there are insufficient constraints to determine the end points r_- and r_+. For example, one can see from the graph that $Q\geqslant 0$ and $L\geqslant 0$ while preserving total Q could also have been achieved by mixing all negative Q from the instability region $r_0<r<r_1$ with positive Q from $r>r_1$. Then $Q=0$ between $r=r_0$ and some $r=r_\star>r_+$ and for $r>r_\star$ Q would be the same as initially (positive). We have to consider L as the primary quantity so that unambiguously $L(r)=\int_0^r Q(r')r'\,\mathrm{d}r'$ (no additional integration constants). Then with the above choice it follows that $L(r_\star)=L(r_0)$. Since r_0 is where the local maximum seen in figure 23(a) occurs, $r_\star$ is simply where a horizontal line tangent to that maximum at $r=r_0$ intersects the L-curve beyond $r=r_+$. Hence for $r_0<r<r_\star$, the proposed L-distribution would everywhere lie above the initial L, while for $r\geqslant r_\star$ and $0\leqslant r<r_0$, L is unchanged. At $r=r_\star$ the velocity field is continuous but not its derivative (Q jumps from 0 to, for example, $Q\approx 1$ if $r_\star$ is large). From this it follows that with this proposed Q-mixing, total L would have increased as well as total kinetic energy, both of which are unacceptable.

Generally we expect that any flow with an L-distribution similar to that shown in figure 15(b) and subsequent figures will adjust in the high-Reynolds-number limit according to the construction discussed here. That is, any simple flow that has positive L everywhere but with an adjacent local maximum and minimum, with inviscid instability guaranteed since $Q<0$ between these extrema, will approach an equilibrium with constant $L=L_c$ in a range that can easily be determined.

As in the anticyclonic case, we may now predict the amount of kinetic energy that would be lost during the equilibration in the $Re\to\infty$ limit. This is shown for both $\alpha=2$ and $\alpha=3$ vortices in figure 25. For $Ro=1.4$ in the $\alpha=3$ case, the hypothetical energy loss is about 3 %, which is very close to what we measured in our $Re=50\times 10^3$ simulations shown in figure 19. For $Ro=4$ the predicted loss is 33 %, whereas in the simulation shown in figure 24 the actual loss is 36 %. For $\alpha=2$, $Ro>2.24$ is required for $\Phi<0$ compared to $Ro>1.01$ when $\alpha=3$, hence the higher Ro-values used in figure 25(a) in the $\alpha=2$ case.

7. Summary and discussion

Based on the experiments discussed above, we have arrived at a theoretical construction that predicts how, in the limit of infinite Re, inertial instability acting alone will stabilize an initially unstable vortex via angular momentum redistribution, preserving total angular momentum. We have found that for vortices that have absolute angular momentum distributions with $L<0$ for some finite range starting at the centre $r=0$, and $L>0$ and monotonically increasing for larger r (as in figure 2b or figure 12a), the equilibrated vortices that emerge from the instability in the high-Reynolds-number limit tend to be determined by the simple construction sketched in figure 12. The prediction is that the equilibrated vortices will have

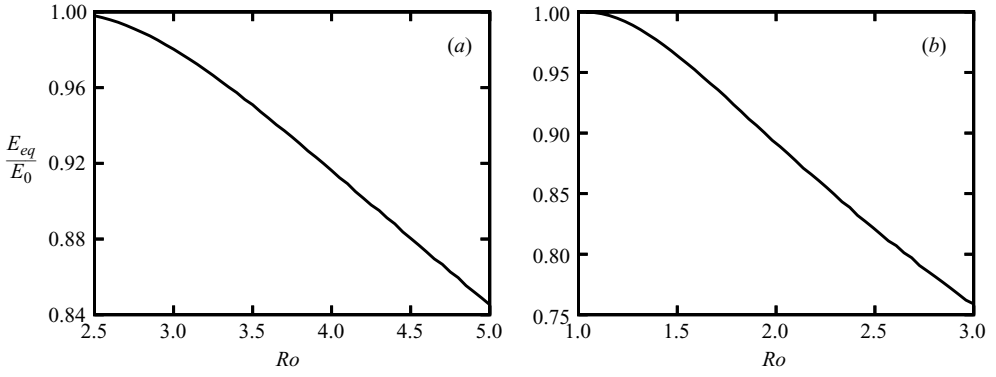

FIGURE 25. The ratio of final equilibrated E_{eq} kinetic energy to initial kinetic energy E_0 as a function of the Rossby number for the hypothetical transition of an unstable cyclonic vortex to the final stable vortex due to inviscid mixing of momentum. Two cases are shown: (*a*) $\alpha = 2$ and (*b*) $\alpha = 3$.

solid-body rotation $\bar{v} = -\frac{1}{2} f r$ from the centre $r = 0$ outwards, with a sharp transition in the $\bar{v}$-field around $r = r_c$ to much smaller velocities. For finite Re, this transition is smooth, but with increasing Re it becomes more rapid and very large gradients in $\bar{L}$ with corresponding large positive $\bar{Q}$ can be established. The extent of the region of solid-body rotation is determined by the requirement that, between $r = 0$ and $r = r_c$, absolute angular moment mixing homogenizes L to $\bar{L} \approx 0$ in that region, thus rendering the equilibrated vortex close to neutrally stable in the inviscid sense ($\Phi \geqslant 0$). Numerical evidence for example shown in figures 10(*b*) and 13(*a*) and additional simulations we have run with different initial velocity distributions indicates that the construction can be applied to a wide variety of vortices as long as the initial L-distribution is of the simple type discussed here.

Vortices with a positive L-distribution such as for example shown in figure 15(*b*) and 23(*a*), adjust in the high-Reynolds-number limit to a stable equilibrium according to the construction shown in 23(*a*). In such flows the instability mixes absolute angular momentum over a range starting to the left of the local maximum (where the region of instability starts) to a point to the right of the local minimum (beyond the region of instability where $Q < 0$). In this range L is homogenized to a constant value L_c which is determined by the constraint that total angular momentum is conserved. In particular the example shown in figure 24(*a*) shows how well the prediction works. In contrast to the anticyclonic flows which re-form with rapid changes in $\bar{L}$ (and corresponding changes in $\bar{v}$), the equilibrated vortices in these cases do not re-form with steep velocity gradients.

These constructions can be applied in more complicated circumstances than discussed above. An illustration of this is given in figure 26 for the case of anticyclones with $\alpha = 10$. Panels (*a*) and (*b*) pertain to the case with $Ro = -0.48$, which is interesting because it is an anticyclone with all L positive, unlike the anticyclones considered above with negative L at small r. In this case, the contruction previously used for anticyclones (figure 12) does not apply. However, we note that the shape of the angular momentum curve is like that of the cyclones considered above and apply the construction sketched in figure 23(*a*) to this anticyclone. This gives the predicted L (thick line in figure 26*a*) and the predicted velocity $\bar{v}$ (thick line in figure 26*b*). It is interesting that the prediction does not give solid-body rotation in the core, as in

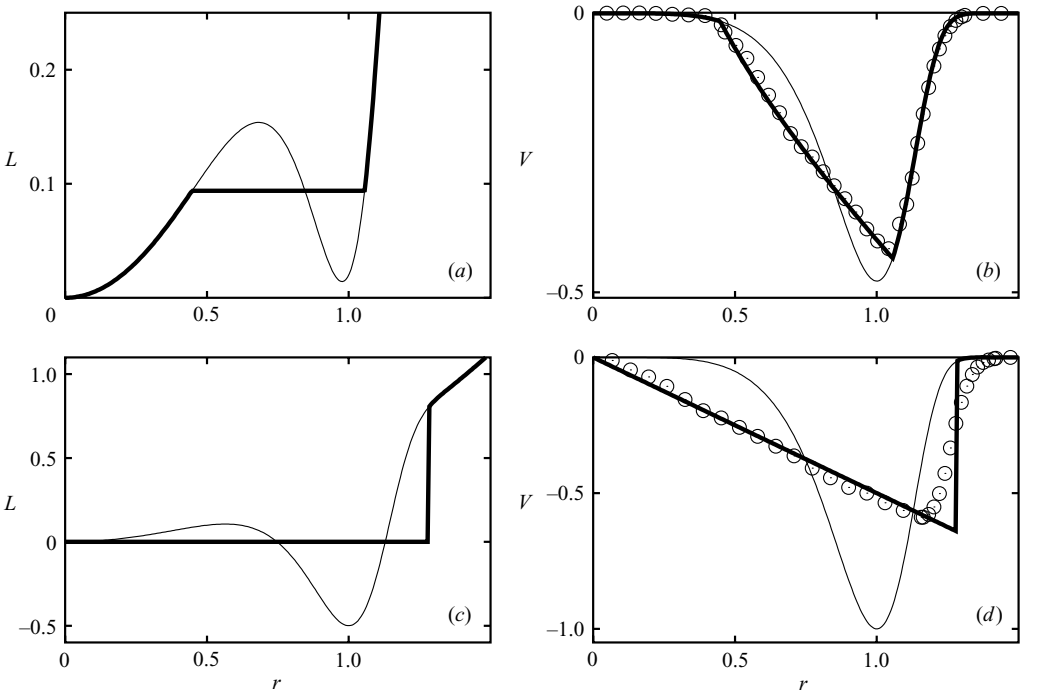

FIGURE 26. Predictions and results for unstable anticyclones with $\alpha = 10$. (*a*) Absolute angular momentum L for the initial conditions (thin) and the prediction (thick) for $Ro = -0.48$. (*b*) The initial velocity profile (thin) V, the predicted velocity profile (thick), the measured $\bar{v}$ at $t = 40$ (circles). (*c*) L for the initial conditions (thin) and the prediction (thick) for $Ro = -1$. (*d*) Initial velocity profile (thin) V, the predicted velocity profile (thick), the measured $\bar{v}$ at $t = 100$ (circles). In both cases $Re = 40 \times 10^3$ and $N = 0$.

all previous anticyclonic cases. Here the redistribution of L does not reach to the axis. The data points in figure 26(*b*) are the vertically averaged velocity at $t = 40$. The flow has rapidly adjusted to the predicted profile. So there are cases in which the construction that we previously applied to cyclones is appropriate to the anticyclone; the initial distribution of L determines which construction is appropriate, not just the sign of Ro.

Figure 26c for the $Ro = -1$ case illustrates another way in which these constructions generalize. Here we have an anticyclone with positive L at small and large r, and negative L between. The total of the positive L at small r alone is insufficient to balance the total negative L, thus some L from higher r must be mixed in to reach a state of $L = 0$. The extension of the construction shown in figure 12 to this case is shown by the thick line in figure 26(*c*). The prediction for the velocity field (thick line in figure *d*) is verified well by the numerical simulation data at $t = 100$.

Decreasing Ro from -0.48 to -1, we pass through a state in which the total negative L is equal in magnitude to the total positive L at small r. In this case both constructions are equivalent if we allow the construction of figure 26(*a*) to be applied even if the local minimum of L has $L < 0$. This simple generalization allows one to pass from one construction to the other smoothly as Ro decreases. Extensions to far more complicated profiles will require further generalization and this will be considered in future work.

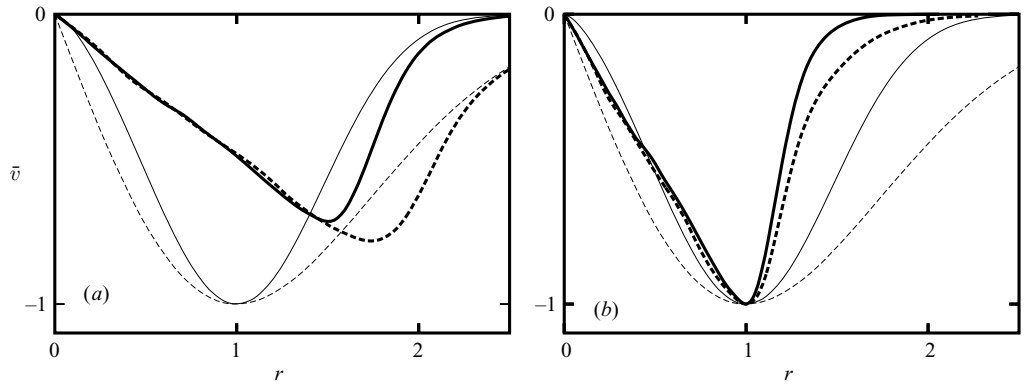

FIGURE 27. (*a*) Equilibrated velocity profiles from simulations with $Re = 10^4$ and $N = 0$ for anticyclones with $Ro = -1$ and $\alpha = 2$ (thick dashed line) and $\alpha = 3$ (thick solid line). Also shown are the initial velocity profiles (thin dashed, $\alpha = 2$; thin solid, $\alpha = 3$). (*b*) Profiles from (*a*) scaled such that in each case the minimum amplitude is -1 at position $r = 1$.

These constructions allow one to estimate how much energy is lost during the adjustment process. It is entirely determined by the kinetic energy contained in the equilibrated flows since negligible amounts of energy are lost through density mixing (potential energy) or internal wave radiation. However, in this study we maintained circular symmetry by suppressing the development of any θ-variations in the fields. It may be that significantly larger losses due to density mixing and wave radiation occur if azimuthal variability is allowed. Also, in that case the vortices may develop barotropic (horizontal shear) instabilities characterized by growing perturbations proportional to $\phi(r)\exp(il\theta)$. In this regard, consider figure 27 where we show the equilibrated anticyclones from numerical simulations both for $\alpha = 2$ and $\alpha = 3$. In figure 27(*a*) the solid-body rotation in the core of the vortices is obvious. Also shown there are the initial profiles. After rescaling such that both have an amplitude $\bar{v} = 1$ at $r = 1$, we see in panel (*b*) that in both cases the profiles have become far steeper after having undergone the inertial instability. Analyses by, for example, Flierl (1988), Carton & McWilliams (1989), Carnevale & Kloosterziel (1994) and many others, have shown that such such steep flow profiles are prone to being barotropically unstable. In contrast, as discussed in § 6.3, for moderate Rossby numbers cyclones are virtually unaltered by inertial instability. When *Ro* is large (figure 24) significant changes occur in that the peak velocity is lowered and the position shifts inwards, affecting the core of the vortex, while the 'tail' of the adjusted velocity profile spans a wider region with velocities higher than initially. It is clear that in this case, if for example the profile shown in figure 24 is rescaled so that the peak velocity and position coincides with the original peak and position, the adjusted profile has become less steep. Thus, unlike the anticyclones, inertially unstable cyclones of the type studied here may emerge barotropically more stable (less steep) after having undergone the inertial instability.

If a vortex is inertially unstable as well as barotropically unstable, both instabilities may occur simultaneously (for studies of the 'competition' between pure inertial instability and the azimuthal (barotropic) shear instabilities, see for example Smyth & McWilliams 1998; Orlandi & Carnevale 1999 and Gallaire & Chomaz 2003). If they occur simultaneously, very chaotic and unpredictable behaviour can ensue, as is easily verified with rotating tank experiments (see Kloosterziel 1990; Afanasyev & Peltier 1998). For example, by simply stirring the rotating fluid in the anticyclonic

direction, one observes (when the Rossby number is negative enough) an explosive inertial instability. Then, as the flow is still in the process of becoming barotropic again (z-independent), almost invariably far from circular, complicated flow patterns are observed (see Kloosterziel & van Heijst 1991; Carnevale & Kloosterziel 1994; Orlandi & Carnevale 1999) which can be thought of as the result of having various azimuthal modes compete (for examples of inertially unstable non-circular vortices showing rather complicated flow evolutions, see Polylitsin & Peltier 2003). From one experiment to the other, even if great care is taken to reproduce the initial conditions, the outcome can vary a great deal. Thus, we believe that to some extent such observations can be explained with our present work, which shows that inertially unstable anticyclones tend to re-form with much steeper profiles than initially which then become barotropically unstable. This scenario is too simple, since typically even when the overturning motions associated with 'pure' inertial instability are still present, one usually observes the first signs of non-circular flow patterns. So, if the constraint of circular symmetry used in the present study is relaxed many possible scenarios for the evolution are possible.

Finally, we should mention here that part of the motivation for the work presented here was the oceanographic observations of anticyclonic eddies that have Rossby numbers close to a value for which $\Phi \geqslant 0$ everywhere. For example, Flament *et al.* (2001) report a detailed observation of a strong anticyclonic eddy which moved southwestward from the island of Hawaii with roughly solid-body rotation $v \approx -\frac{1}{2}fr$ in the core up to the velocity peak. They surmized that this eddy had undergone inertial instability prior to the observations since this sets $\Phi \geqslant 0$ everywhere. The present study suggests that they were correct.

R.C.K. acknowledges support from the National Science Foundation (grants OCE 01-28991 and 05-26033), G.F.C. acknowledges support from the National Science Foundation (grants OCE 01-29301 and 05-25776), the Ministero Istruzione Universita e Ricerca (MIUR D.M. 26.01.01 n. 13) and the San Diego Supercomputer Center. The authors thank Dr W. H. Schubert of Colorado State University for providing us with a translation of Solberg's (1936) paper.

REFERENCES

Afanasyev, Y. D. & Peltier, W. R. 1998 Three-dimensional instability of anticyclonic flow in a rotating fluid: Laboratory experiments and related theoretical predictions. *Phys. Fluids* **10**, 3194–3202.

Billant, P. & Gallaire, F. 2005 Generalized Rayleigh criterion for non-axisymmetric centrifugal instabilities. *J. Fluid Mech.* **542**, 365–379.

Carnevale, G. F., Briscolini, M., Kloosterziel, R. C. & Vallis, G. K. 1997 Three-dimensionally perturbed vortex tubes in a rotating flow. *J. Fluid Mech.* **341**, 127–163.

Carnevale, G. F., Briscolini, M. & Orlandi, P. 2001 Buoyancy to inertial range transition in forced stratified turbulence. *J. Fluid Mech.* **427**, 205–239.

Carnevale, G. F. & Kloosterziel, R. C. 1994 Emergence and evolution of triangular vortices. *J. Fluid Mech.* **259**, 305–331.

Carton, X. & McWilliams, J. C. 1989 Barotropic and baroclinic instabilities of axisymmetric vortices in quasi-geostrophic model. In *Mesoscale/Synoptic Coherent Structures in Geophysical Turbulence* (ed. J. C. J. Nihoul & B. M. Jamart), pp. 225–244. Elsevier.

Drazin, P. & Reid, W. 1981 *Hydrodynamic Stability*. Cambridge University Press.

Fjørtoft, R. 1950 Application of integral theorems in deriving criteria of stability for laminar flows and for the baroclinic vortex. *Geofys. Publ.* **17** (6), 5–52.

Flament, P., Lumpkin, R., Tournadre, J. & Armi, L. 2001 Vortex pairing in an unstable anticyclonic shear flow: discrete subharmonics of one pendulum day. *J. Fluid Mech.* **409**, 401–409.

Flierl, G. R. 1988 On the instability of geostrophic vortices. *J. Fluid Mech.* **197**, 349–388.

Gallaire, F. & Chomaz, J.-M. 2003 Three-dimensional instability of isolated vortices. *Phys. Fluids* **15**, 2113–2126.

Griffiths, S. D. 2003*a* The nonlinear evolution of of zonally symmetric equatorial inertial instability. *J. Fluid Mech.* **474**, 245–273.

Griffiths, S. D. 2003*b* Nonlinear vertical scale selection in equatorial inertial instability. *J. Atmos. Sci.* **60**, 977–990.

Hua, B. L., le Gentil, S. & Orlandi, P. 1997*a* First transitions in circular Couette flow with axial stratification. *Phys. Fluids* **9**, 365–375.

Hua, B. L., Moore, D. W. & Le Gentil, S. 1997*b* Inertial nonlinear equilibration of equatorial flows. *J. Fluid Mech.* **331**, 345–371.

Jacquin, L. & Pantano, C. 2002 On the persistence of trailing vortices. *J. Fluid Mech.* **471**, 159–168.

Kloosterziel, R. C. 1990 Barotropic vortices in a rotating fluid. PhD thesis, University of Utrecht.

Kloosterziel, R. C. & van Heijst, G. J. F. 1991 An experimental study of unstable barotropic vortices in a rotating fluid. *J. Fluid Mech.* **223**, 1–24.

Ooyama, K. 1966 On the stability of the baroclinic circular vortex: a sufficient condition for instability. *J. Atmos. Sci.* **23**, 43–53.

Orlandi, P. 2000 *Fluid Flow Phenomena: A Numerical Toolkit*. Kluwer.

Orlandi, P. & Carnevale. G. F. 1999 Evolution of isolated vortices in a rotating fluid of finite depth. *J. Fluid Mech.* **381**, 239–269.

Potylitsin, P. G. & Peltier, W. R. 1998 Stratification effects on the stability of columnar vortices on the f-plane. *J. Fluid Mech.* **355**, 45–79.

Potylitsin, P. G. & Peltier, W. R. 2003 On the nonlinear evolution of columnar vortices in a rotating environment. *Geophys. Astrophys. Fluid Dyn.* **97**, 365–391.

Rayleigh, Lord 1916 On the dynamics of revolving fluids. *Proc. R. Soc. Lond.* A **93**, 148–154.

Sawyer, S. J. 1947 Notes on the theory of tropical cyclones. *Q. J. R. Met. Soc.* **73**, 101–126.

Shen, C. Y. & Evans, T. E. 1998 Inertial instability of large Rossby number horizontal shear flows in a thin homogeneous layer. *Dyn. Atm. Oceans* **26**, 185–208.

Smyth, W. D. & McWilliams, J. C. 1998 Instability of an axisymmetric vortex in a stably stratified, rotating environment. *Theor. Comp. Fluid Dyn.* **11**, 305–322.

Smyth, W. D. & Peltier, W. R. 1994 Three-dimensionalization of barotropic vortices on the f-plane. *J. Fluid Mech.* **265**, 25–64.

Solberg, H. 1936 Le mouvement d'inertie de l'atmosphere stable et son role dans la theorie des cyclones. *Sixth Assembly, Edinburgh.* Union Geodesique et Geophysique Internationale, pp. 66–82.

Stone, P. H. 1966 On non-geostrophic stability. *J. Atmos. Sci.* **23**, 390–400.

van Heijst, G. J. F. & Kloosterziel, R. C. 1989 Tripolar vortices in a rotating fluid. *Nature* **338**, 569–571.

van Heijst, G. J. F., Kloosterziel, R. C. & Williams, C. W. M. 1991 Laboratory experiments on the tripolar vortex in a rotating fluid. *J. Fluid Mech.* **225**, 301–331.

Yanai, M. & Tokiaka, T. 1969 Axially symmetric meridional motions in the baroclinic circular vortex: a numerical experiment. *J. Met. Soc. Japan* **47** (3), 183–197.